REMOTE SENSING STUDIES OF THE SCHILLER-SCHICKARD REGION OF THE MOON

A THESIS SUBMITTED TO THE GRADUATE DIVISION OF THE UNIVERSITY OF HAWAII IN PARTIAL FULFILLMENT OF THE REQUIREMENTS FOR THE DEGREE OF

MASTER OF SCIENCE

IN

GEOLOGY & GEOPHYSICS

DECEMBER 1994

By

David Taylor Blewett

Thesis Committee:

B. Ray Hawke, Chairperson
Jeffrey F. Bell
Paul G. Lucey
G. Jeffrey Taylor

We certify that we have read this thesis and that, in our opinion, it is satisfactory in scope and quality as a thesis for the degree of Master of Science in Geology and Geophysics.

THESIS COMMITTEE

Bernard Ray Hawke
Chairperson

Jeffrey D. Bell

Paul Lucey

ACKNOWLEDGMENTS

The author wishes to express gratitude to the following individuals: Mark Robinson, for teaching me almost everything I know about image processing and for his patience and helpfulness while doing so, and for getting me to appreciate the VAX; Harold Garbeil for computer help on innumerable occasions; Karl Hinck for computer help; Jim Bell for consulting on the early spectral mixing models and for showing me how to use S-Plus to make spectral plots; Chris Peterson for discussions of the finer points of band analysis; Greg Smith for his expertise in SPECPR; Michelle Tatsumura for advice on the Celco (filmwriter); Charles Budney for lunar discussions and computer advice; Bruce Campbell for some early help with images and for being a great housemate; James Granahan for various technical advice; Kevin Polk for sundry assistance in the Data Center; Lorna Ramiscal, Charlotte Albert-Thenet, Meredith Lee and Stacy Fong of the Hawaii Space Grant College for being wonderful co-workers and keeping the undergraduate fellowship program running smoothly despite my occasional lapses; all the other students, staff and faculty of the Planetary Geosciences Division for making PGD a wonderful place to work; Henning Haack and Scott Rowland for going body boarding; and Gina Ling for everything.

This work was supported by a graduate fellowship from the Hawaii Space Grant College (Peter Mouginis-Mark, director) and by NASA grant NAGW-237 (B. Ray Hawke, principal investigator).

TABLE OF CONTENTS

TABLE OF CONTENTS (Continued)

LIST OF TABLES

LIST OF FIGURES

LIST OF FIGURES (Continued)

CHAPTER 1
INTRODUCTION

"Under blue moon I saw you ... "
[*Echo & the Bunnymen*, 1984]

The surface of the Moon can be divided into two major physiographic provinces: rugged regions of high albedo and generally high elevation, and smoother, darker low-lying plains. These are the familiar highlands, which dominate the farside and the central and southern portions of the nearside, and the maria, which fill in the lowlands, commonly within the nearside basins. The highlands are understood to be the heavily-cratered feldspar-rich remnants of the primary lunar crust [*Taylor*, 1989], while the maria represent a secondary crust composed of basaltic lava flows that flooded much of the nearside somewhat later in lunar history. There is another type of landform found on the Moon which, though not as extensive as the highlands or maria, is widespread and covers significant areas (some 4-7% of the nearside - *Oberbeck et al.*, 1974). This landform has been given various names: light plains, Imbrian-age plains, terra plains, smooth plains, and Cayley plains. The light plains are distinguished by albedae intermediate between those of the highlands and the maria. They are smooth and often appear to have ponded to a level surface in depressions. The number density of craters found on the light plains is greater than that of the mare but less than that of the highlands [*Eggleton and Schaber*, 1972], implying an intermediate age.

The origin of the light plains has been the subject of much controversy. Early geologic mappers interpreted the light plains to be volcanic deposits. The smooth, level nature of the plains along with their moderate albedo suggested ash sheets or unusual low viscosity lavas of possibly silicic composition (e.g., *Milton and Hodges* [1972]). The Cayley Formation in the central highlands of the nearside was the type example of a light plains deposit, and the Apollo 16 landing site was chosen largely to investigate

the Cayley plains. When the rocks collected by the Apollo 16 astronauts were found to be non-volcanic breccias, there was a scramble to find an interpretation of light plains consistent with the new sample evidence.

In the time since the end of the Apollo era, it has become evident that several modes of origin are required to explain the lunar light plains [*Blewett et al.*, 1993; *Head et al.*, 1993b]. A few occurrences of light plains, such as those found within Orientale, are likely to be assemblages containing much impact melt [*Head*, 1974]. Another phenomenon which may contribute to the formation of light plains is the tremendous input of seismic energy from a basin-forming impact. *Schultz and Gault* [1975] found that surface waves would arrive contemporaneously with ejecta at a range of ~1000 - 2000 km from an Orientale basin-sized impact. The surface waves could induce landsliding and fluidization of the ejecta materials, resulting in leveling of the deposit. An hypothesis explaining light plains as the product of viscous leveling caused by unusual heat flow conditions early in lunar history [*Bastin*, 1974] has not been widely accepted.

Although the importance of volcanism was far overestimated prior to the return of lunar samples, there are instances of light plains units that were probably produced by extrusive volcanism. The Apennine Bench Formation [*Hackman*, 1966], located along the edge of the Imbrium basin and near the Apollo 15 site, was mapped as an archetypal light plains unit [*Wilhelms and McCauley*, 1971]. Work in the last 15 years, drawing on information from photogeology, lunar samples, orbital geochemistry, and Earth-based remote sensing, has demonstrated that the Apennine Bench probably represents a large expanse of non-mare volcanic material [*Hawke and Head*, 1978; *Spudis*, 1978; *Spudis et al.,* 1988]. An alternative to the volcanic origin for the Apennine Bench, proposed by *Deutsch and Stöffler* [1987], holds that it is a mega-slump block within the Imbrium cavity.

Additionally, the role of impact processes in the formation of light plains has been reevaluated, and the influence of basin-forming impacts beyond the continuous basin ejecta has been recognized [*Oberbeck et al.,* 1975a,b; *Oberbeck*, 1975]. The work by Oberbeck and coworkers emphasizes the role of ballistic erosion and sedimentation in lunar stratigraphy, and particularly in the formation of the distal deposits of impact basins. The model (also known as the local mixing hypothesis) considers secondary cratering to be a major process in modifying and redistributing material on the lunar surface. In the Oberbeck model, the ejecta curtain produced by a basin-forming impact gives rise to a fluidized mass of material that moves away from the target point along the surface as a debris surge. This debris surge is the result of the impact of secondary crater-forming projectiles, and consists of both primary (basin) ejecta and material derived from the substrate. A key unresolved question concerns the relative amounts of primary ejecta and local material incorporated into the resulting deposit.

A major subtype of the debris surge-derived light plains is that produced by the burial of mare basalts [*Schultz and Spudis*, 1979]. A hidden mare deposit of this kind has been referred to as a "cryptomare" [*Head and Wilson*, 1992]. Areas of buried mare basalts are identified primarily by the occurrence of dark-haloed impact craters (DHC's). For example, in the region of craters Schiller and Schickard in the southwestern portion of the nearside, near-infrared reflectance spectroscopy has been used to show that the dark-halo craters present there excavate mare basalt from beneath a higher albedo surface unit rich in highlands debris [*Hawke and Bell*, 1981; *Bell and Hawke*, 1984; *Blewett et al.,* 1991, 1992].

The Schiller-Schickard region (Figures 1.1, 1.2, 1.3) is the focus of the research described herein. This area contains a number of interesting geologic features. These include the crater Wargentin, whose floor is topographically higher than the surrounding terrain; the elongated crater Schiller; the Schiller-Zucchius impact basin

[*Hartmann and Wood*, 1971]; the large crater Schickard (227 km diameter), whose floor contains mare deposits as well as a light plains unit; and several other light plains units, some with associated DHC's. A sketch map of major features in the area is shown in Figure 1.4. This research aims to further elucidate the nature and origin of lunar light plains and their association with the cryptomaria. Cryptomaria, such as those in the Schiller-Schickard region, present a unique opportunity to test the ballistic erosion model of basin ejecta emplacement. This is possible because of the presence of a spectrally distinct substrate (mare basalt) which can be detected as a component of the highlands-like basin deposit. The validity of the local mixing hypothesis has implications for the modes of emplacement of distal basin deposits elsewhere on the Moon, the provenance of lunar samples, and the interpretation of orbital geochemical data. I have used near-infrared reflectance spectra and multispectral images to investigate the composition of surfaces in the Schiller-Schickard region, and compared the results with the predictions of the local mixing hypothesis.

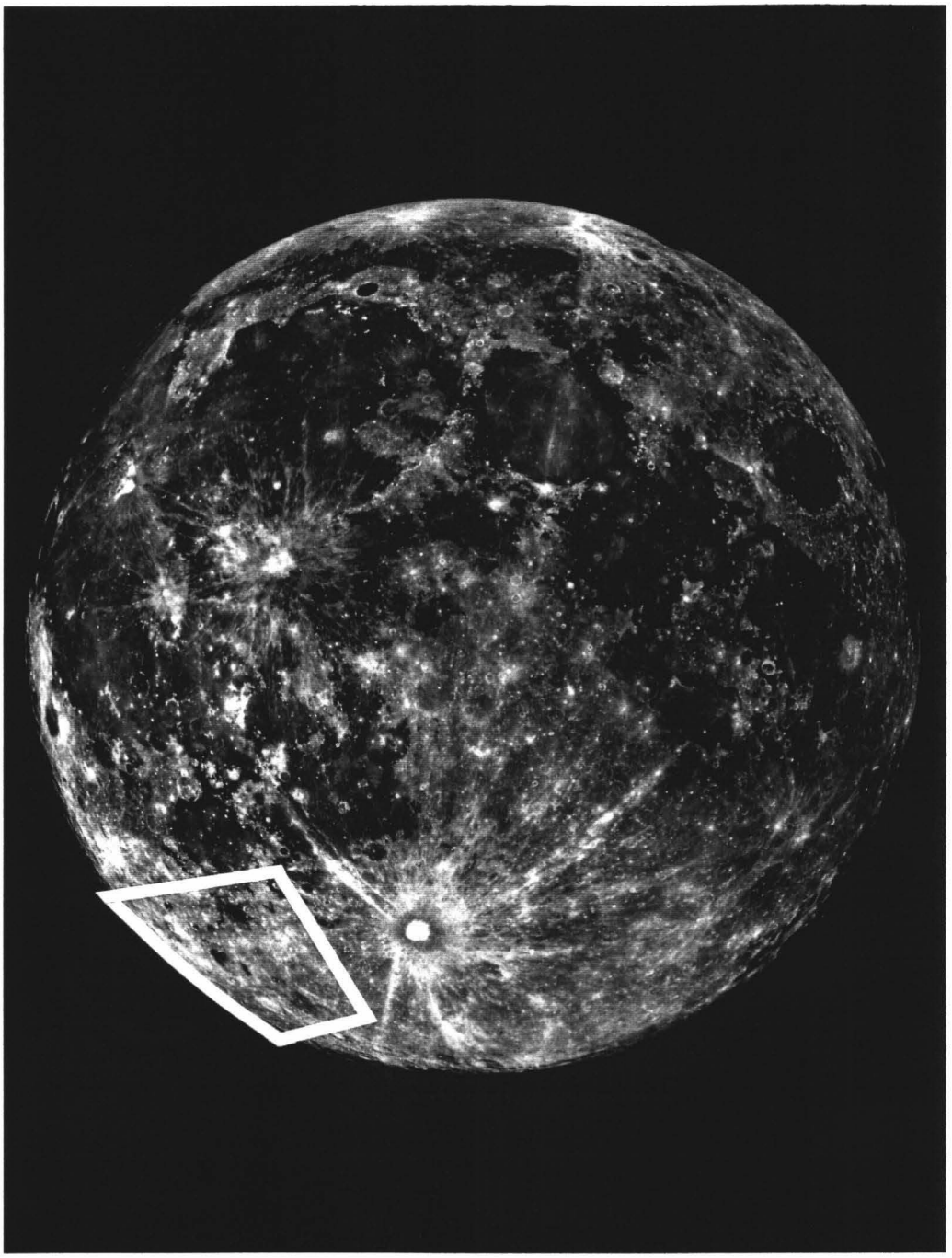

Figure 1.1. Full-Moon photograph showing the location of the Schiller-Schickard region. The box approximates the area shown in Figures 1.2 and 1.3.

Figure 1.2. Rectified Earth-based telescopic photo of the Schiller-Schickard region at high Sun angle (part of Plate 23-c of *Whitaker et al.* [1963]). Selected dark-haloed impact craters are indicated by the arrows. North is to the top. Scale ≅ 41 km/cm. For identification of features refer to the sketch map in Figure 1.4.

Figure 1.3. Rectified Earth-based telescopic photo of the Schiller-Schickard region at low Sun angle (part of Plate 23-d of *Whitaker et al.* [1963]). North is to the top. Scale ≅ 41 km/cm. For identification of features refer to the sketch map in Figure 1.4.

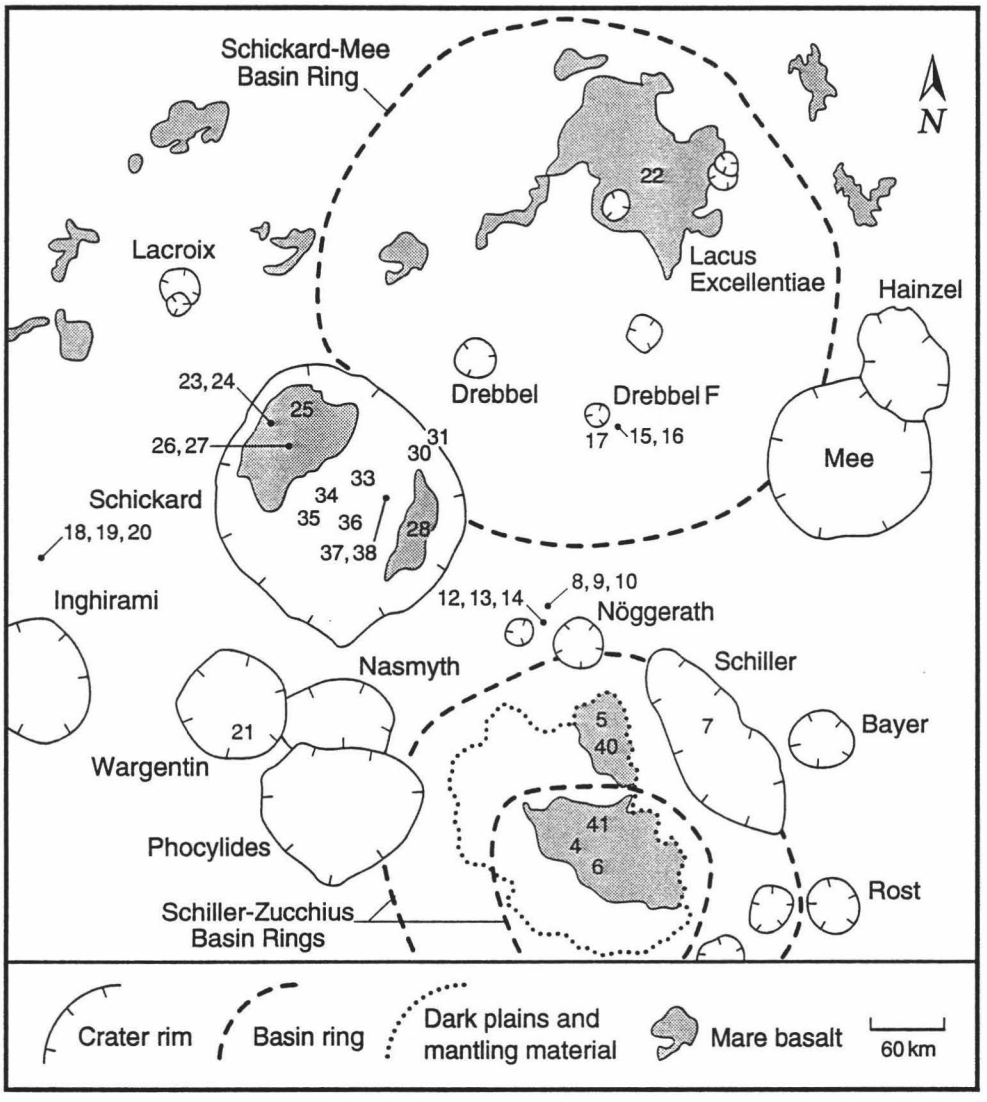

Figure 1.4. Geologic sketch map of the Schiller-Schickard region. Major features discussed in the text are shown. Numbers correspond to locations for which near-IR reflection spectra were obtained, as listed in Table 2.1.

CHAPTER 2
ANALYSIS OF NEAR-INFRARED REFLECTANCE SPECTRA

"I am scattering like light ... "
[*Vega*, 1985]

2.1 Introduction

Near-infrared (near-IR) reflectance spectra for the nearside of the Moon have been collected by Planetary Geosciences observers since the late 1970's (see *McCord et al.* [1981] for a summary of early work). These spectra, collected systematically with specific goals in mind, are a valuable resource for attacking problems in lunar science. Spectra for features in the Schiller-Schickard (SS) region from this database were assembled into a study set and analyzed with two quantitative techniques: band analysis and principal components analysis. This chapter describes the observations, the analysis procedures, and the results thereof.

2.2 Astronomical Observations

The majority of the near-infrared reflectance spectra used in this study were recorded with the Planetary Geosciences InSb spectrometer mounted on the University of Hawaii 2.24 m telescope on Mauna Kea. A small number of spectra were obtained with a 61 cm telescope. The spectrometer instrument successively measures the intensity of light in 120 channels between 0.6 and 2.5 μm by rotating a filter with a continuously variable band pass in front of the detector. Circular apertures in the telescope focal plane admit Moonlight to the detector; aperture sizes of 0.7 or 2.3 arcsec were employed. The resulting spot sizes on the lunar surface were ~1.5 or ~4.5 km in average diameter under optimum observing conditions. Observational and data reduction techniques were standard, and details can be found elsewhere [*McCord et al.*,

1981]. The spectral data were manipulated by use of an interactive computer program developed by *Clark* [1980].

2.3 Analysis Procedures

2.3.1 Band Analysis

Iron-bearing pyroxenes are responsible for an absorption band in lunar spectra near 1 μm. The shape and position of this band provide information on the composition of the pyroxene (*Adams*, 1974]. In order to extract this information, the method of *Lucey et al.* [1986] was employed. First, a straight line is fit to the reflectance "peaks" on either side of the "1 μm" band (usually near 0.7 and 1.6 μm; refer to Figure 2.1). The slope of this line (Δ scaled reflectance/Δλ) defines a useful spectral parameter, the continuum slope. Next, the continuum is removed by dividing the spectrum by the continuum line. The shape of the absorption band in the resulting continuum-removed spectrum is modeled by fitting it with a cubic polynomial (Figure 2.2). The equation of the polynomial in conjunction with lines fit to the sides of the band yield four band parameters: the band's wavelength position of the reflectance minimum, full width at half-maximum depth (FWHM), and asymmetry (Figure 2.3). The asymmetry parameter, not discussed by *Lucey et al.* [1986], is the ratio of the semi-width of the band shortward of the minimum to the semi-width longward of the minimum.

Of principal interest for determining mineralogy are the position of the band minimum and the band depth. Spectra for mare basalt surfaces have deep bands with minima at >0.95 μm, indicating high-Ca pyroxene. The low-Ca orthopyroxenes of highlands mineral assemblages produce bands with minima shortward of 0.95 μm. Over thirty-five spectra for features in the SS region were obtained, including mature mare surfaces, mare craters, dark-halo crater interior and ejecta deposits, light plains surfaces, and a highlands crater. Selected representative spectra are shown in Figures 2.4-2.6, and derived spectral parameters are listed in Table 2.1. The spectra have not

been corrected for thermal emission, and some spectra show effects of incomplete removal of atmospheric water absorptions near 1.4 and 1.9 μm. Some of the names of the spectra as shown in Table 2.1 have been modified from the name given at the time that the observations were made. This was done to simplify the discussion in the text and to maintain consistency in the names of the spectra. The original names of the spectra as they appear in the Planetary Geosciences database are provided in a table in Appendix A, along with the dates of the observations.

The uncertainty in the positions of the band minima given in Table 2.1 is not easily quantified, and depends on the quality of the spectrum under consideration. The polynomial fit to the band considers only the reflectance value, and not the range of values represented by the error bars. Thus a study of the uncertainty could be made for each spectrum by randomly shifting each data point within the error bars, then re-calculating the polynomial and band minimum. While this would be an interesting project, it is probably not actually necessary. This is because the position of the band minimum is only one of several pieces of information used in the mineralogical interpretation of a spectrum. Equally important are the continuum slope, the band depth, and photogeologic knowledge of the area for which the spectrum was collected. If the only data available was a list of band minima, then a rigorous knowledge of the uncertainty would be very important. A qualitative idea of the uncertainty in the location of the band minimum is given by experience in working with spectra. Often in attempting to fit a spectrum, a number of trials are made to fit the polynomial. In each trial, slightly different portions of the spectrum in the vicinity of the "1 μm" band are selected for fitting with the polynomial (i.e., a different number of spectral channels are used for the fit). This exercise shows that in no case does the determined location of the band minimum change enough to alter the mineralogical interpretation Typically, the change is in the third decimal place. For example, a first try might yield a band

Table 2.1. Spectral parameters derived for Schiller-Schickard spectra.

Spectrum ID no.	Spot Name	Band min. (μm)	Continuum slope	Band depth	FWHM* (μm)	Asymmetry
3	Apollo 16					
4	Schiller-Zuc Plains S	0.959	0.627	0.060	0.352	0.651
5	Schiller-Zuc Plains N	0.980	0.625	0.060	0.280	0.894
6	Schiller-Zuc Plains #3	0.950	0.676	0.066	0.261	0.631
7	Schiller floor	0.929	0.604	0.061	0.248	0.610
8	Noggerath F bowl #1	0.975	0.529	0.217	0.280	0.786
9	Noggerath F bowl #2	0.969	0.496	0.205	0.276	0.827
10	Noggerath F bowl #3	0.976	0.551	0.189	0.281	0.871
12	Nogg F ejecta #1	0.978	0.662	0.112	0.253	0.932
13	Nogg F ejecta #2	0.969	0.666	0.120	0.248	0.750
14	Nogg F ejecta #3	0.991	0.650	0.084	0.223	1.159
15	Drebbel F ejecta #1	0.948	0.644	0.061	0.260	0.667
16	Drebbel F ejecta #2	0.976	0.664	0.068	0.264	0.926
17	Drebbel F ejecta #3	0.954	0.667	0.050	0.213	0.947
18	Inghirami W	0.976	0.661	0.071	0.277	0.854
19	Inghirami W bowl #1	0.985	0.602	0.106	0.264	1.140
20	Inghirami W bowl #2	0.946	0.590	0.141	0.291	0.719
21	Wargentin DHC	0.994	0.646	0.052	0.282	1.529
22	Lacus Excellentiae	0.973	0.640	0.076	0.287	0.777
23	Schickard mare N #1	0.970	0.691	0.086	0.288	0.721
24	Schickard mare N #2	0.962	0.702	0.083	0.229	0.759
25	Schickard mare N #3	0.978	0.695	0.082	0.251	1.038
26	Schickard mare crater #1	0.961	0.641	0.148	0.269	0.831
27	Schickard mare crater #2	0.989	0.611	0.133	0.292	1.338
28	Schickard mare S	0.996	0.690	0.088	0.292	0.773
30	Schickard X #1	0.958	0.526	0.062	0.326	0.802
31	Schickard X #2	0.920	0.486	0.053	0.189	0.871
33	Schickard R	0.976	0.672	0.095	0.276	0.842
34	Schickard center	0.944	0.630	0.048	0.298	0.774
35	Schickard LP #1	0.935	0.605	0.051	0.222	0.657
36	Schickard LP #2	0.956	0.598	0.048	0.228	0.900
37	Schickard LP crater #1	0.959	0.436	0.201	0.270	0.862
38	Schickard LP crater #2	0.962	0.618	0.120	0.327	0.807
40	Schiller-Zuc Plains #4	0.955	0.595	0.081	0.287	0.789
41	Schiller-Zuc Plains #5	0.952	0.654	0.073	0.266	0.482

*Full width at half maximum

minimum at 0.933 μm, and a second try 0.938 μm. Therefore, I would estimate the uncertainty in a quoted wavelength position of band minimum as ±0.01 μm.

2.3.2 Principal Components Analysis

In order to gain further insight into the data set, the multivariate statistical technique of principal components analysis (PCA) was applied. A method of using PCA for spectral data was developed by *Smith et al.* [1985] and applied to lunar telescopic and sample spectra by *Johnson et al.* [1985] and *Pieters et al.* [1985]. More recently, *Jaumann* [1991] utilized PCA in a study of lunar sample laboratory spectra and their relationship to chemical composition. PCA reduces the dimensionality of the data to a small number of factors related to the causes of the variation, aiding in the selection of spectral endmembers and revealing mixing trends. To apply PCA to the SS spectra, a computer program to perform the statistical calculations described by *Smith et al.* [1985] was written in the IDL language (see Appendix B) and checked with example data sets from chapter 6 of *Davis* [1986]. Twenty-five of the highest quality SS spectra were selected for inclusion in the PCA. Portions of the spectra in the vicinity of telluric water bands (near 1.4 and 1.9 μm) and longward of 2 μm (thermal contamination) were not included in the analysis. The spectra thus were defined by reflectances at 69 wavelengths between 0.67 and 1.81 μm. A laboratory spectrum of an Apollo 16 soil sample which represents the spectrum of the Apollo 16 standard telescopic observing site [*McCord et al.*, 1981] was also included in the PCA. The Apollo 16 standard site is an excellent spectral match for the western limb highlands [*Hawke et al.*, 1991]. Absolute albedo information is not preserved in the telescopic observations, so the spectra were all scaled to 1.0 at 1.02 μm.

The variance-covariance matrix of the spectral data matrix was calculated, and the eigenvectors and eigenvalues extracted. The eigenvalues are shown in Table 2.2. The ratio of each eigenvalue to the total sum of the eigenvalues represents the proportion of variance contained in that principal component. These ratios are sometimes referred to as the principal component loadings, and are also given in Table 2.2.

Table 2.2. Eigenvalues and principal component loadings for the first four principal components determined for the Schiller-Schickard spectra.

PC Axis Number	Eigenvalue	% of Total Variance
1	0.1203	75.9
2	0.0320	20.2
3	0.0025	1.6
4	0.0008	0.5

In the present case, the first two principal components are responsible for over 96% of the variation in the data. The relationship of the principal components to physically meaningful quantities may be examined by plotting the eigenvectors against wavelength. The eigenvector spectra of Figure 2.7 show that the first principal component is mainly related to the position and depth of the "1 μm" band. The second principal component is sensitive to the spectral slope. Similar interpretations of eigenvector spectra were made by *Johnson et al.* [1985] and *Jaumann* [1991]. Principal component scores for the near-IR spectra are calculated by transforming each spectrum by the eigenvectors of Figure 2.7. This is accomplished by summing the products of the eigenvector and the reflectance for all wavelengths in the spectrum, i.e.,

$$PC_i = \sum E_{i,\lambda} \cdot R_\lambda$$

where PC_i = principal component score of spectrum on *i*th PC axis
$E_{i,\lambda}$ = value of *i*th eigenvector at wavelength λ
R_λ = reflectance value of spectrum at wavelength λ.

Each spectrum may then be located as a single point in PC space (Figure 2.8). In this plot, the spectral endmembers are found at the extremes, and mixtures lie within the boundaries [*Smith et al.*, 1985]. Our observations included four possible endmembers - mature and fresh mare, and mature and fresh highlands. It can be seen in Figure 2.8 that these are well separated by the PCA, plotting approximately at the endpoints of a four-sided figure. Spectra of mixtures of these four, such as dark-halo crater material and light plains surfaces, reside within the area defined by the endmembers. The single point away from the main group, labeled "37", represents a spectrum of a small extremely fresh crater in the Schickard light plains. The extreme freshness of this crater, which exposes a mixture of highlands and mare material, imparts a very deep absorption band and very shallow continuum slope to the spectrum. Therefore it is not a reasonable endmember to consider for the present group of spectra.

The contribution of each endmember to a mixture spectrum can be calculated from the distance of a mixture from each of the endmembers in Figure 2.8. For the present purpose, linear mixing of spectral endmembers [*Singer and McCord*, 1979] is assumed. A linear ("checkerboard") model describes the mixture of components on a macroscopic scale (~centimeter or greater). In other words, multiple scattering of photons is ignored. A linear model is adequate because lunar materials are generally of low albedo and produce little multiple scattering. Also, the study of lunar spectral mixing by *Johnson et al.* [1985] has shown that results from a linear mixing model do not differ greatly from those assuming nonlinear (intimate) mixing.

Because the mixing model is based on normalized spectra, the abundances represent the contribution of each endmember to the total *flux* of the modeled mixture spectrum. In order to determine the actual *area* fractions of the endmembers on the lunar surface, the flux fractions must be weighted by the albedos of the endmembers. This is accomplished with the following relationship:

$$\frac{A_i a_i}{\sum_{j=1}^{n} A_j a_j} = f_i \qquad (2.1)$$

where A_i = area fraction of endmember i,
a_i = albedo of endmember i
f_i = flux fraction of endmember i .
n = number of endmembers

Because the spectral observations do not provide information on albedo, it is necessary to use another source. Previous workers have often used the normal albedo maps produced by *Pohn and Wildey* [1970] or *Wildey* [1977]. However, the spectra used in the present analysis were scaled to 1.0 at 1.02 μm, so it is necessary to use the albedos of the endmembers at 1.02 μm, whereas the effective wavelength of the *Pohn and Wildey* [1970] and *Wildey* [1977] maps is 0.55 μm. Also, the resolution of the hard copy [*Pohn and Wildey*, 1970] and digital [*Wildey*, 1977] maps are too low to accurately locate points near the limb, where the SS region is found. Therefore a digital telescopic image of the SS region at 0.99 μm (see discussion in Chapter 3) was used to provide relative albedo values.

2.4 Results and Discussion

2.4.1 Highlands

To investigate the composition of the pre-Orientale highlands material in the Schiller-Schickard region, two spectra were obtained for Schickard X, an 8 km crater in the eastern wall of Schickard (Figures 1.2, 1.3 , 1.4). The walls and bowl of this crater should expose highlands material from beneath any Orientale-related deposits. One spectrum (no. 31 in Table 1) has a band minimum at 0.92 μm, a shallow continuum slope of 0.49, and a weak 5% depth. These spectral parameters are consistent with an Fe^{+2}-bearing plagioclase-rich assemblage, with low-Ca pyroxene as the dominant mafic

mineral. The lithology indicated is a noritic anorthosite. This composition is very common in the southern and western highlands, being similar to that at the Apollo 16 landing site and to that found in much of the exterior deposits of Orientale (Hevelius Formation) [*Hawke et al.*, 1991]. A second spectrum (no. 30) has a band minimum slightly longward, at 0.96 μm, though the slope (0.53) and depth (6%) are similar to the first. This spectrum was collected with a smaller aperture. Photographs taken during the course of data collection indicate that the elliptical "footprint" of the aperture on the lunar surface, elongated by the location of the target near the limb, included a small amount of mare basalt-bearing area on the floor of Schickard. This is the probable explanation for the longer band minimum. The results of the PCA indicate that the area for which the spectrum was obtained is dominated by noritic anorthosite with minor amounts of mare basalt (note the location of this spectrum in Figure 2.8).

2.4.2 Mare Units

Near-IR reflectance spectra were also collected for a variety of mare units in the SS region. These include spectra for mature surfaces on the north and south mare patches within Schickard (numbered 23-25, and 28 in Table 1), and for a mare unit northeast of Schickard in Lacus Excellentiae (no. 22). In addition, two observations of a small crater in the Schickard north mare were made (no.s 26 and 27). These spectra have band minima in the range 0.96 to 1.0 μm. The mature surfaces typically have band depths of ~8%, while the fresh rock surfaces exposed in mare craters yield spectra with depths of 13-15%. The continuum slopes of the mature mare (~0.7) are slightly steeper than those for the craters (~0.6). The parameters are characteristic of a mafic mineral assemblage dominated by high-Ca pyroxene.

2.4.3 Dark-Halo Craters

The DHC's Drebbel F, Inghirami W, Nöggerath F, and Schickard R were shown by *Bell and Hawke* [1984] and *Hawke and Bell* [1981] to have mare basalt signatures, demonstrating that the dark haloes are indeed due to exposed mare basalt. Detailed analysis of the spectra of these craters, including spectra not considered in the previous reports, has been carried out. The results, along with data for another DHC in the region, are discussed below.

Several separate observations of the bowl (no.s 8-10) and ejecta (no.s 12-14) of crater Nöggerath F (48.0°S, 46.9°W; 9 km diam.) were made. The band minima for these spectra range from 0.97 to 0.99 μm. The bowl of the crater exposes fresh basalt, indicated by the deep bands (19-22%) and less-steep continuum slopes (~0.5). The band depths and continuum slopes of the spectra obtained for the ejecta of Nöggerath F, as well as the location of the ejecta spectra in PC space (Figure 2.8), indicate that the basaltic ejecta has not reached the level of maturity of the mare surfaces within Schickard.

Inghirami W (44.4°S, 67.4°W; 6.5 km diam.) is found to the west of Schickard, in the continuous deposits of Orientale. Two spectra were collected for the bowl of Inghirami W (no.s 19 and 20), in addition to one spectrum that included both the bowl and the dark halo (no. 18). One bowl spectrum was fairly noisy, making the position of band minimum uncertain. The higher quality spectrum yielded a band minimum of 0.99 μm. The determined band depths and continuum slopes for both bowl spectra were similar to each other and very much like that of local mare craters. The dark halo spectrum exhibits a minimum at 0.98 μm. The continuum slope and band depth are consistent with a greater level of maturity present in the halo material. Inghirami W clearly exposed mare basalt from beneath the highlands-rich unit emplaced as a result of the Orientale impact event.

Three spectra (no.s 15-17) of areas on the dark ejecta of Drebbel F crater (42.7°S, 44.6°W; 15 km diam.) have band minima between 0.95 and 0.98 μm, consistent with a basaltic regolith. The values for continuum slope and band depth are slightly less than those for nearby mature mare surfaces. It appears that the dark halo of Drebbel F is dominated by mare basalt with small and variable amounts of highlands debris. A smaller unnamed crater has penetrated the northeast rim of Drebbel F and could have contributed some less mafic material to the exterior deposits.

A single large aperture spectrum was collected for Schickard R, a 5-km diameter DHC in the Schickard light plains. The observation (no. 33 in Table 2.1) included the crater bowl and dark halo, as well as some of the light plains [*Hawke and Bell*, 1981]. The spectral parameters are almost identical to those of mature areas on the nearby mare patches on the floor of Schickard. This crater has definitely excavated mare basalt.

The 84 km diameter crater Wargentin, just to the southwest of Schickard, has an unusual morphology. Wargentin has a flat floor well above the level of the surrounding terrain and approximately level with the lowest point in the crater wall. A ridge similar to those found on mare surfaces crosses the raised floor, which has a highlands-like albedo. A spectrum of the prominent DHC on the southern portion of the floor of Wargentin has a band minimum at 0.99 μm, definitely showing that mare basalt exists beneath the light plains unit. This confirms the hypothesis of *Hawke and Bell* [1981] that Wargentin was filled with extrusive volcanic material, then covered with a layer of higher-albedo material as a result of the Orientale impact event.

2.4.4 Light Plains and Cryptomaria

Data gathered by the solid state imaging system onboard the *Galileo* spacecraft during the first Earth-Moon encounter has been used to identify a large region in and around Schickard with an enhanced mafic mineral content relative to the surrounding

highlands [e.g., *Belton et al.*, 1992; *Head et al.*, 1993a]. The higher mafic abundance has been interpreted by the Galileo team to reveal the modification and burial of pre-Orientale mare deposits by Orientale ejecta. Extensive portions of this cryptomare correlate with light plains deposits in the SS region.

In order to better understand the nature and origin of the light plains units in the Schiller-Schickard region, near-IR reflectance spectra obtained for small areas on the light plains were analyzed. On the basis of qualitative comparison of absorption band depths, *Bell and Hawke* [1984] proposed that the light plains on the floors of Schickard and Schiller craters contain a large component of pyroxene-rich material. The spectral parameters derived in the present work allow more detailed analysis. The parameters for three spectra of areas on the light plains on the floor of Schickard (no.s 34-36) are given in Table 2.1. The band minima range from 0.94 to 0.96 μm, indicating the presence of some high-Ca pyroxene. The strengths of the absorption bands in these spectra (5%) are slightly greater than expected for a typical mature highlands surface. The continuum slope, 0.6, also is intermediate between that of mature highlands and mature mare spectra.

Light plains are also found on the floor of Schiller crater. A spectrum of this deposit (no. 7) has characteristics resembling those of the Schickard light plains. The minimum is at 0.93 μm, slightly shortward of those for the Schickard light plains, and the continuum slope of 0.6 is the same. However, the band depth of 6% suggests the presence of either a fresher surface or a slightly higher amount of mafic minerals. Since photographs of the area for which the spectrum was obtained show no fresh craters, a more mafic composition is indicated.

The spectra for the Schickard light plains and the plains on the floor of Schiller lie along a mixing line between mature mare (Schickard mare north #2, no. 24) and mature highlands (Apollo 16, no. 3) on the PC space plot of Figure 2.8. A two-component

mixing analysis for the plains spectra was performed by measuring the distance of each mixture from the two endmembers in Figure 2.8. For example, the proportion of endmember 1 is given by the ratio (distance from mixture to endmember 2)/(distance from endmember 1 to endmember 2). The proportion of endmember 2 = (distance from mixture to endmember 1)/(distance from endmember 1 to endmember 2) = (1-proportion of endmember 1). A comparison of the original spectra and model spectra created by mixing the proportions of endmember spectra determined by PCA is shown in Figure 2.9 along with the RMS error. The model spectra fit the observed data quite well, with overall errors being ~1%. To convert the flux fractions in the spectra to area abundances on the lunar surface, the DN values of an area on the northern mare unit within Schickard and a spot on the Hevelius formation in the 0.99 μm CCD image (discussed in Chapter 3) were used as the mature mare and mature highlands endmember albedae in Eqn. 2.1. The results of the conversion to area abundances are given in Table 2.3.

The mixing model indicates that significant amounts of mare basalt are found in the Schickard light plains, varying from ~40-67% depending on the spot observed. This is in accord with the expectations from the band analysis. Similarly, the light plains within Schiller are shown to contain ~70% basalt. [The results for spectra nos. 5 and 6 (Schiller-Zucchius plains) are discussed in section 2.4.5.]

Table 2.3. Two-endmember spectral mixing model results based on PCA for light plains and related surfaces in the SS region.

Spectrum ID no.	Spot Name	Mature Highl. (%)	Mature Mare (%)
5	Schill-Zuc Pl. N	18	82
6	Schill-Zuc Pl. #3	15	85
7	Schiller Floor	30	70
34	Schick. Center	59	41
35	Schick. LP #1	41	59
36	Schick. LP #2	33	67

The spectra of the Schickard and Schiller light plains units discussed above were derived from observations of the mature upper surfaces of these deposits and clearly demonstrate the presence of major amounts of mare material. Is this mare component present throughout the light plains or just at the surface? An enrichment of mare basalt only in the surface could be explained by vertical impact mixing between a "pure" highlands layer overlying a substrate of mare basalt. Impacts penetrating the highlands layer would excavate mare material and distribute it on the surface, forming dark-haloes around the craters. As this process was repeated, the mare content of the surface would increase, though the interior of the plains unit would contain little mare. An enrichment throughout the depth of the light plains would be expected if a local mixing process had operated during the emplacement of the plains. In order to differentiate between these two possibilities, two spectra were obtained for a small (~1.4 km diam.) very fresh unnamed crater in the Schickard light plains. This impact crater excavated material from a variety of depths within the light plains unit. A crater with this diameter should be approximately 280 m deep (assuming a 1:5 depth:diameter relationship [*Pike*, 1974]). However, the vast majority of the ejecta was derived from the upper 140 m of the pre-impact target site [*Stöffler et al.*, 1975]. Although the thickness of the Schickard light plains deposit is variable, it is well over 200 m thick in the area where this small crater formed (e.g., *Antonenko and Head* [1994]), so the material excavated and re-deposited by the impact originated in the interior of the light plains unit. The composition of the fresh crater material should provide important information concerning the lithology of the subsurface portions of the Schickard light plains. The spectrum (no. 38) recorded for the small crater and its ejecta blanket exhibits a relatively strong absorption band (~12%) with a band minimum near 0.96 μm. The spectral parameters indicate the presence of a sizable mare component in the area for which the spectrum was obtained. A second spectrum (no. 37) was collected for the

interior of the crater. This spectrum also has a band minimum near 0.96 μm, but the band is stronger (~20%) and the continuum slope is very shallow. The crater interior contains a large amount of mare basalt.

In order to determine the amount of mare material present within the light plains unit, a mixing analysis based on PCA was conducted for the spectrum obtained for the interior and exterior deposits of the small crater. The results of a two-component (fresh mare, fresh highlands) mixing model indicated that the crater deposits contain 44% immature mare material. A three-component (fresh mare, fresh highlands, mature highlands) yielded similar results: 46% immature mare basalt. These results clearly show that mare basalt is a major component in the material that makes up the Schickard light plains. Mare basalt is present throughout the entire thickness of the deposit, and is not just enriched in the regolith. This finding supports local mixing as the process responsible for incorporating mare basalt as a component of the light plains unit. Section 3.3 of the next chapter also examines evidence bearing on the origin of the mare component in the Schiller-Schickard light plains.

2.4.5 Schiller-Zucchius Plains

The Schiller-Zucchius plains (which correspond in part to the "Schiller Plains" of *Offield* [1971]) lie to the west and southwest of Schiller crater and occupy a portion of the Schiller-Zucchius basin (Figures 1.2, 1.3, 1.4). This area, which has a lower albedo and crater density than the surrounding highlands, has been previously mapped as "dark plains" and attributed to ash deposits [*Offield*, 1971]. However, the material of the Schiller-Zucchius plains exhibits mare-type ridges which are roughly radial to Orientale, appears to embay the adjacent terrain, and floods some small ruined craters. These morphologic characteristics are more consistent with post-Orientale mare basalt flows than pyroclastic deposits. Five telescopic observations were made to gain compositional information for surfaces on the Schiller-Zucchius plains (no.s 4-6, 40,

and 41). The spectra have bands with minima from 0.95-0.98 μm and depths of 6-8%; the continuum slopes are 0.60-0.68. Thus the spectra are indicative of mare basalt, though some of the band depths are slightly less and the positions of some of the minima are slightly shortward of the values determined for spectra of the mare patches in Schickard. The likely explanation for these spectral parameters is a minor admixture of highlands material contaminating a post-Orientale mare surface. Mixing analysis conducted on two of the Schiller-Zucchius plains spectra (similar to that described above) shows that a combination of ~15% highlands debris with 85% mare material can provide a good match (Figures 2.8 and 2.9, Table 2.3). The 64-km diameter Copernican-age crater Zucchius is located ~250 km to the southwest. Zucchius rays and secondary craters are found on the Schiller-Zucchius plains [*Offield*, 1971; *Hawke and Bell*, 1981], making Zucchius the likely chief source of the highlands contamination.

Crater statistics presented by *Greeley et al.* [1993] indicated a model age of 3.70 Ga for the Schiller-Zucchius plains. Figure 11 of *Greeley et al.* [1993] shows the area labeled "Schiller-Zucchius plains" for which crater counts were made. However, close examination of available Lunar Orbiter photography and consultation with the map of *Offield* [1971] clearly shows that small areas of Orientale secondary crater cluster material were included in the area mapped as Schiller-Zucchius plains by *Greeley et al.* [1993]. These workers noted that the model age of 3.7 Ga is younger than the Orientale and Imbrium impacts, and that it is unlikely that the Schiller-Zucchius plains can be attributed to material emplaced as a result of these basin-forming events. They suggested that the plains may be ejecta deposits of adjacent, younger craters, such as Zucchius, or possibly of other origin.

The results of our analysis suggest a fairly straight-forward origin for the Schiller-Zucchius plains. Mare basalts were emplaced at ~3.70 Ga. These lavas embayed

adjacent terrain and flooded pre-existing Orientale secondary craters. The wrinkle ridges that are generally radial to Orientale may have been formed by the flooding of Orientale secondary crater chains and clusters that are roughly radial to the basin. These mare deposits were subsequently contaminated by a minor amount of highlands debris transported to the area as a consequence of the Zucchius and other impact events [*Blewett et al.*, 1992]. We thus restrict the term "Schiller-Zucchius plains" to indicate the post-Orientale mare deposits near Schiller that have received minor highlands contamination.

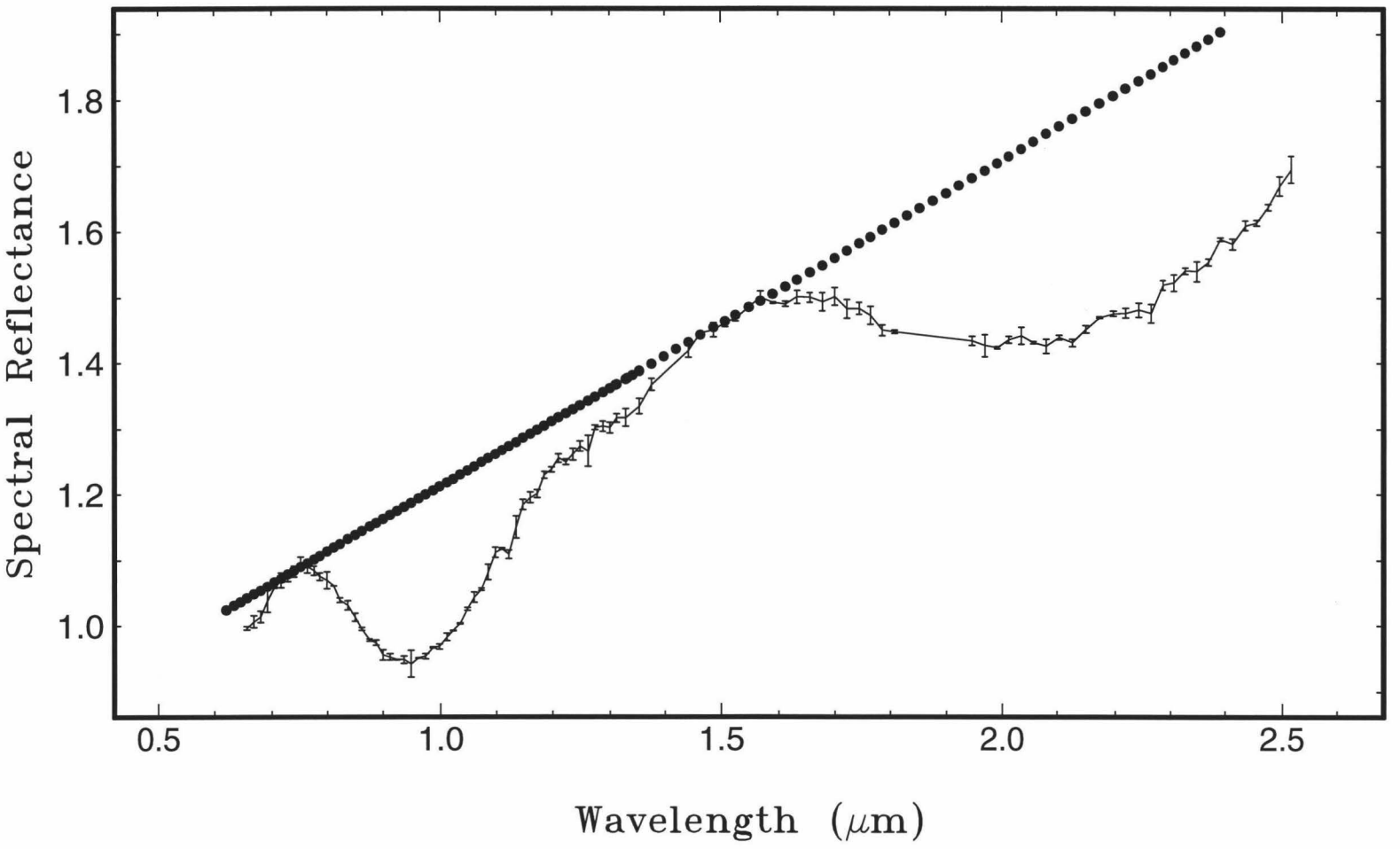

Figure 2.1. Example of the fitting of a continuum line to a lunar near-IR reflectance spectrum. The spectrum shown is for Nöggerath F bowl (Table 2.1 and Figure 2.4).

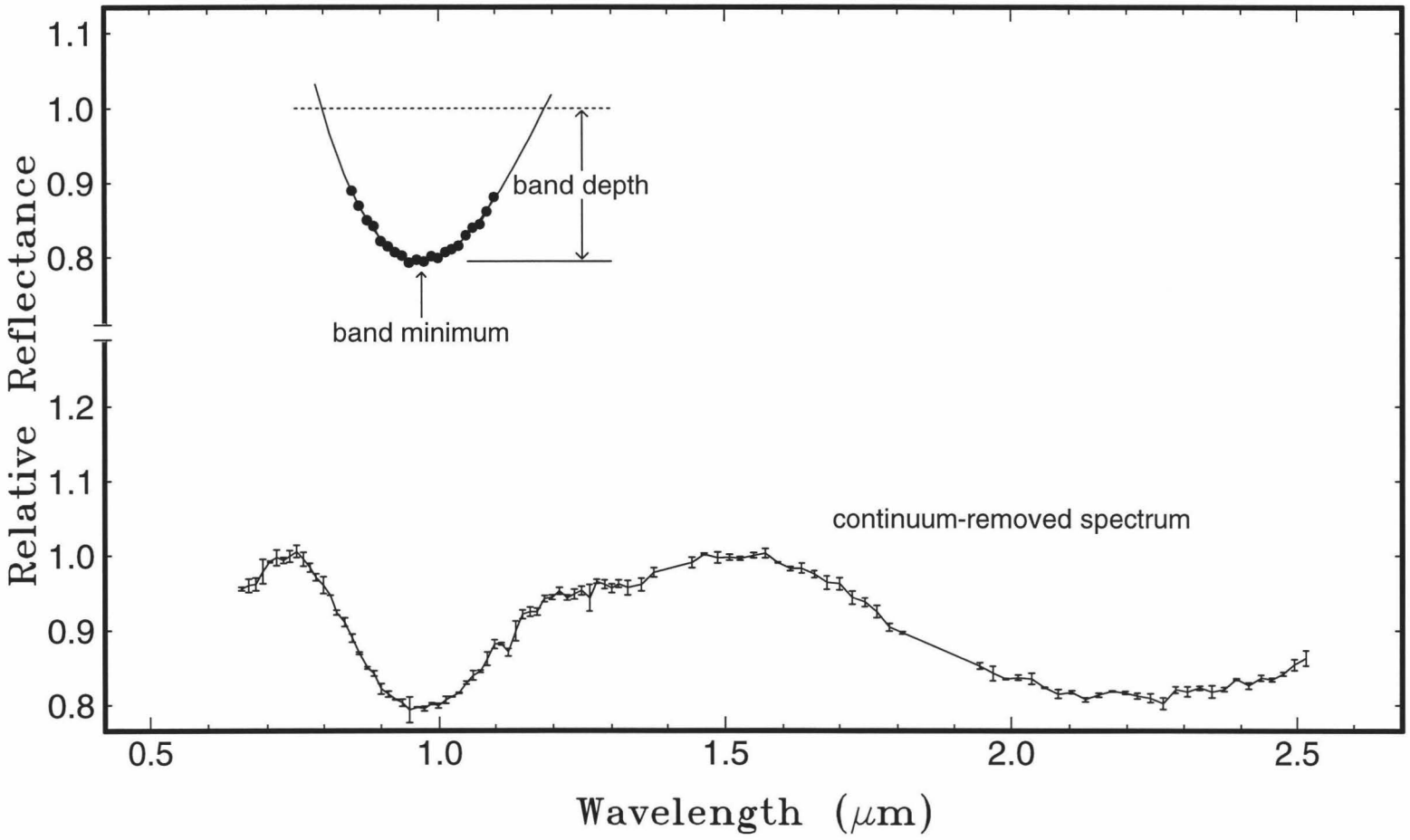

Figure 2.2. Illustration of steps in the analysis of the "1 μm" absorption band. The lower portion of the graph shows the result of dividing the spectrum in Figure 2.1 by the continuum line. The uppper portion of the graph shows the fitting of a cubic polynomial (solid line) to the lower part of the absorption band in the continuum-removed spectrum (dots).

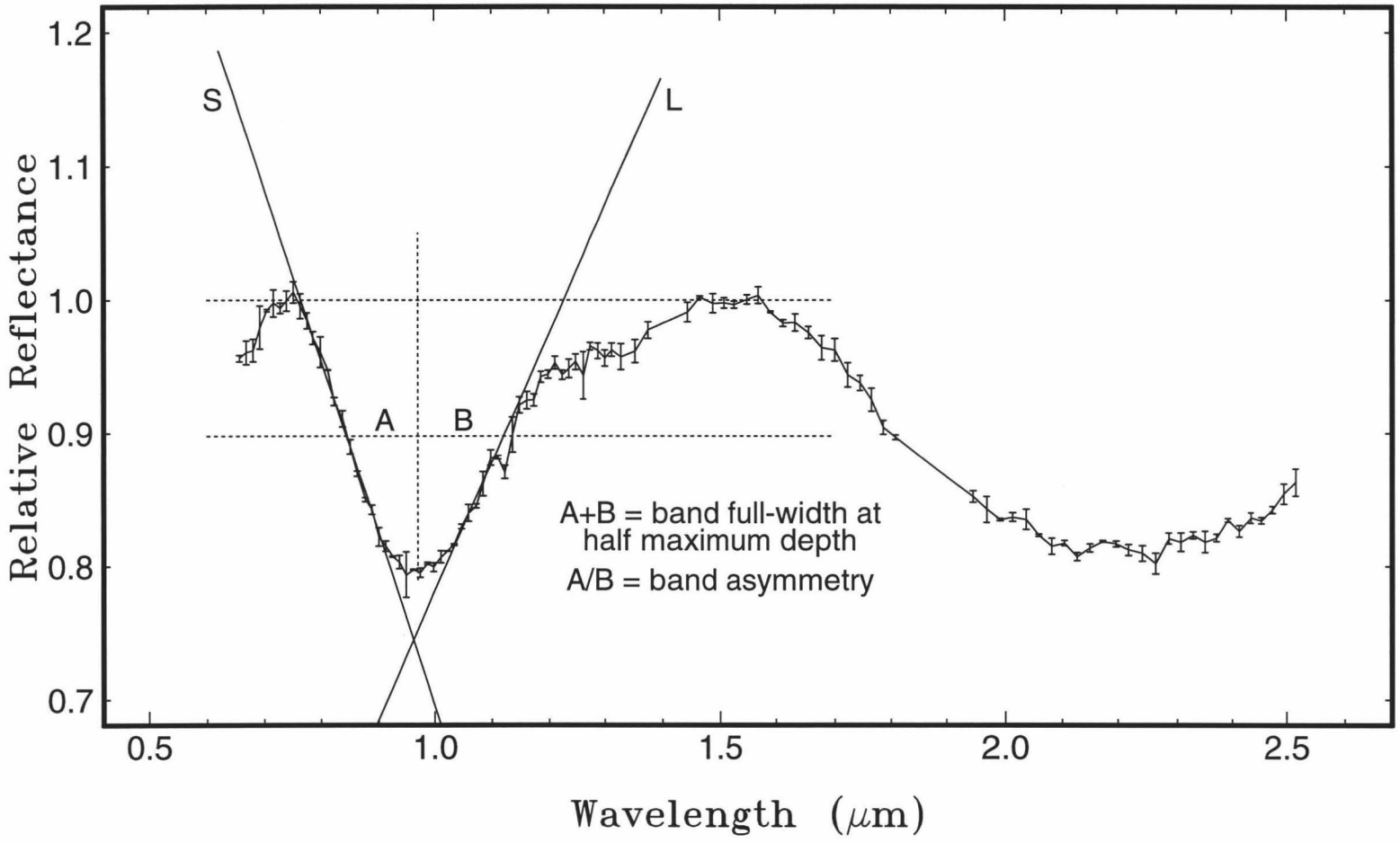

Figure 2.3. Determination of the band width and asymmetry. The solid lines labeled S and L are lines fit to the short and long wavelength sides of the band in the continuum-removed spectrum. The vertical dashed line is located at the wavelength position of the reflectance minimum. The lower horizontal dashed line is drawn at the band's half depth. The lengths of the segments A and B yield the band's full width at half maximum (FWHM) and asymmetry parameter.

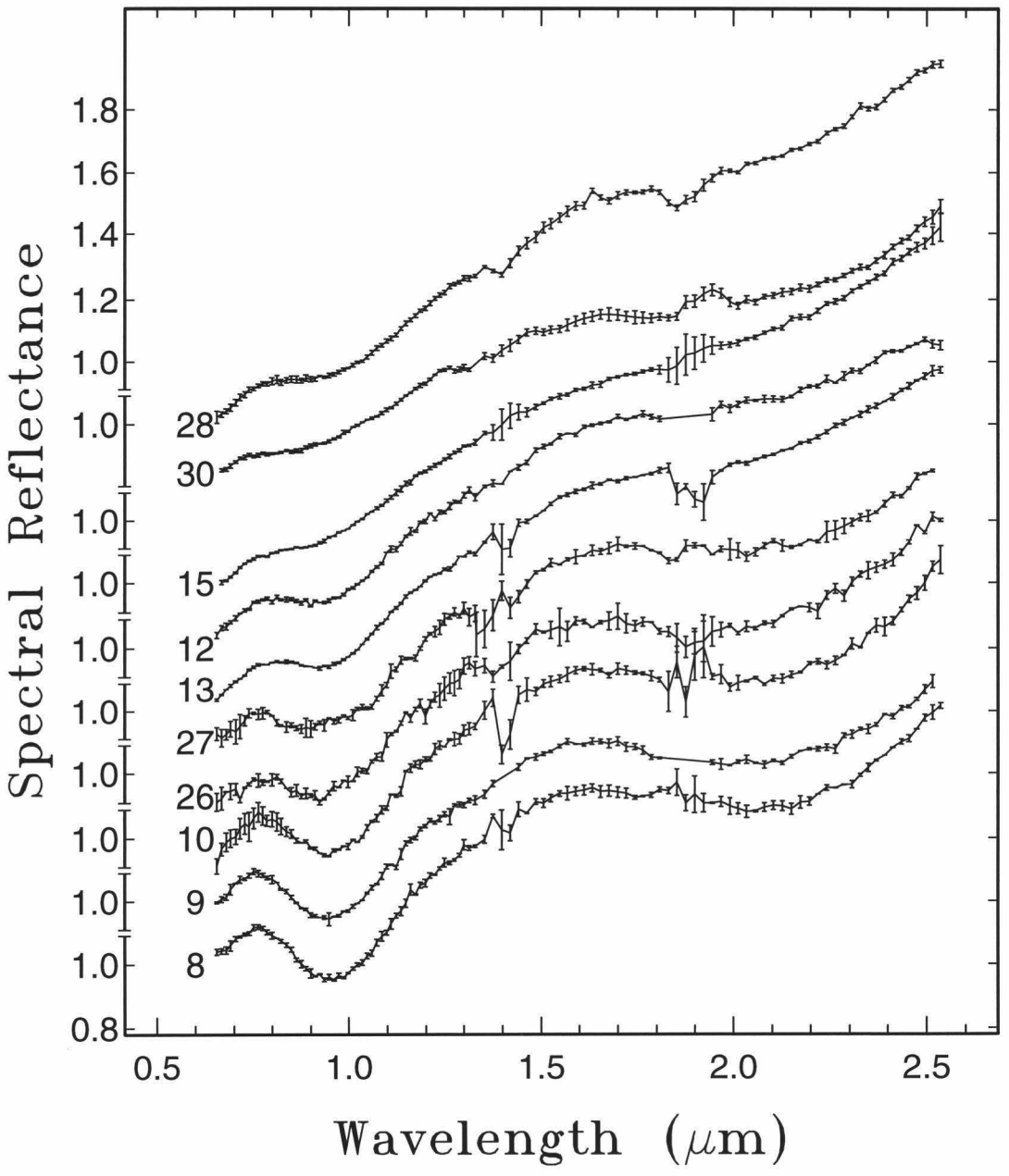

Figure 2.4 (a). Near-IR reflectance spectra (spectra/Sun, scaled to 1.0 at 1.02 μm) for some of the locations given in Figure 1.4 and listed in Table 2.1. These spectra, and those of Figures 2.5 and 2.6, have been offset for clarity.

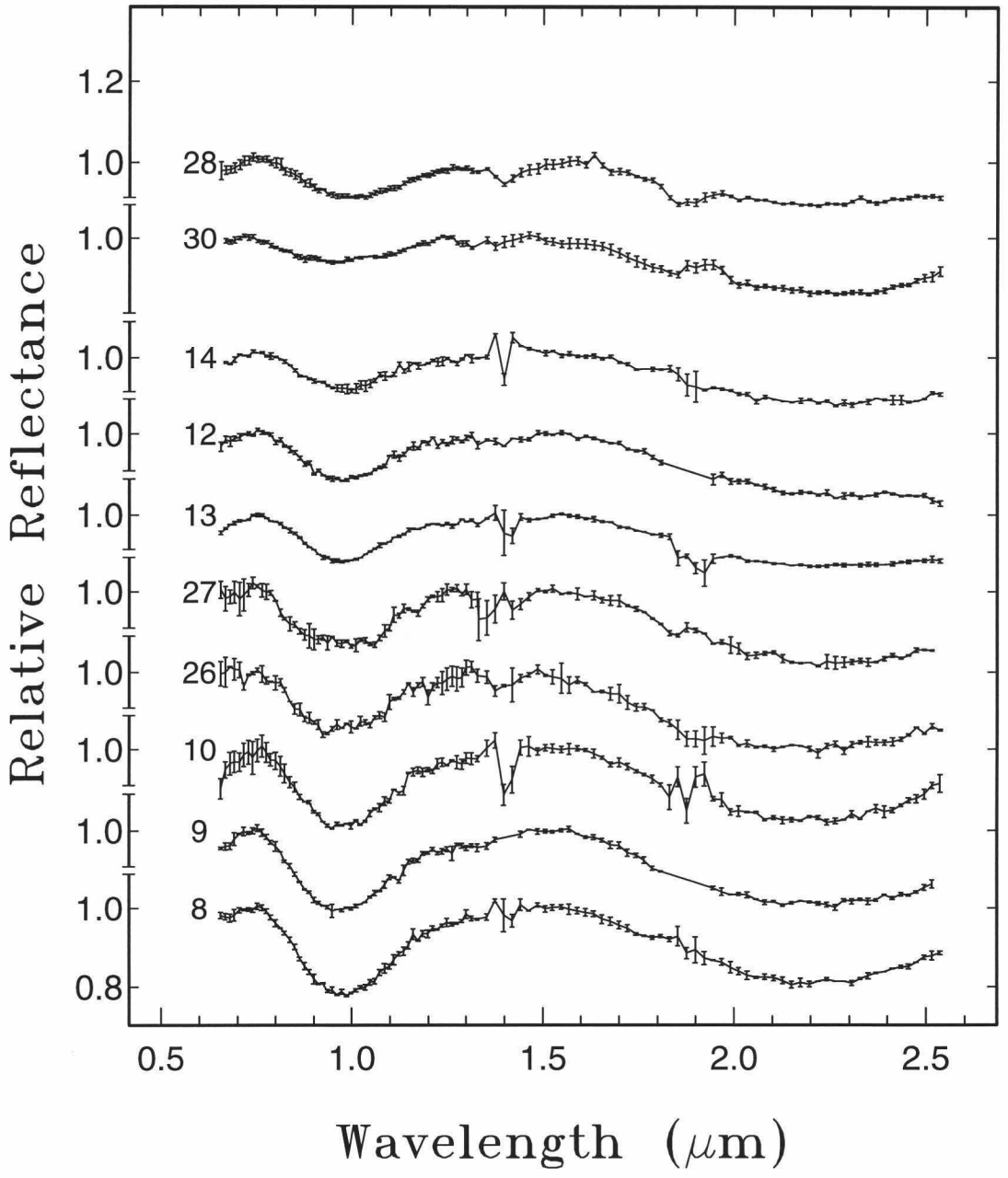

Figure 2.4 (b). Continuum removed versions of the spectra shown in Figure 2.4(a). These spectra, and those of Figures 2.5 and 2.6, have been offset for clarity.

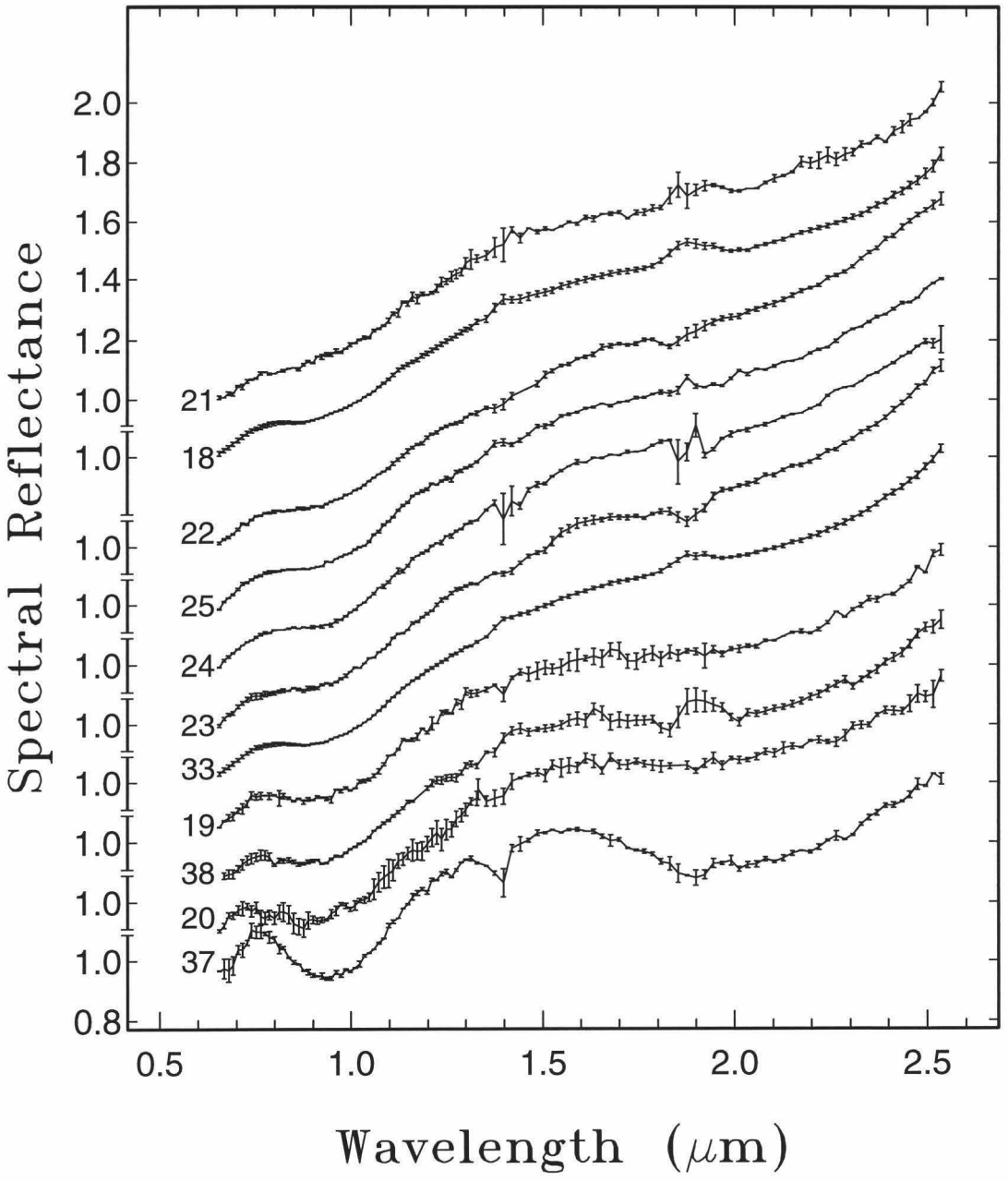

Figure 2.5 (a). Near-IR reflectance spectra (spectra/Sun, scaled to 1.0 at 1.02 μm) for some of the locations given in Figure 1.4 and listed in Table 2.1.

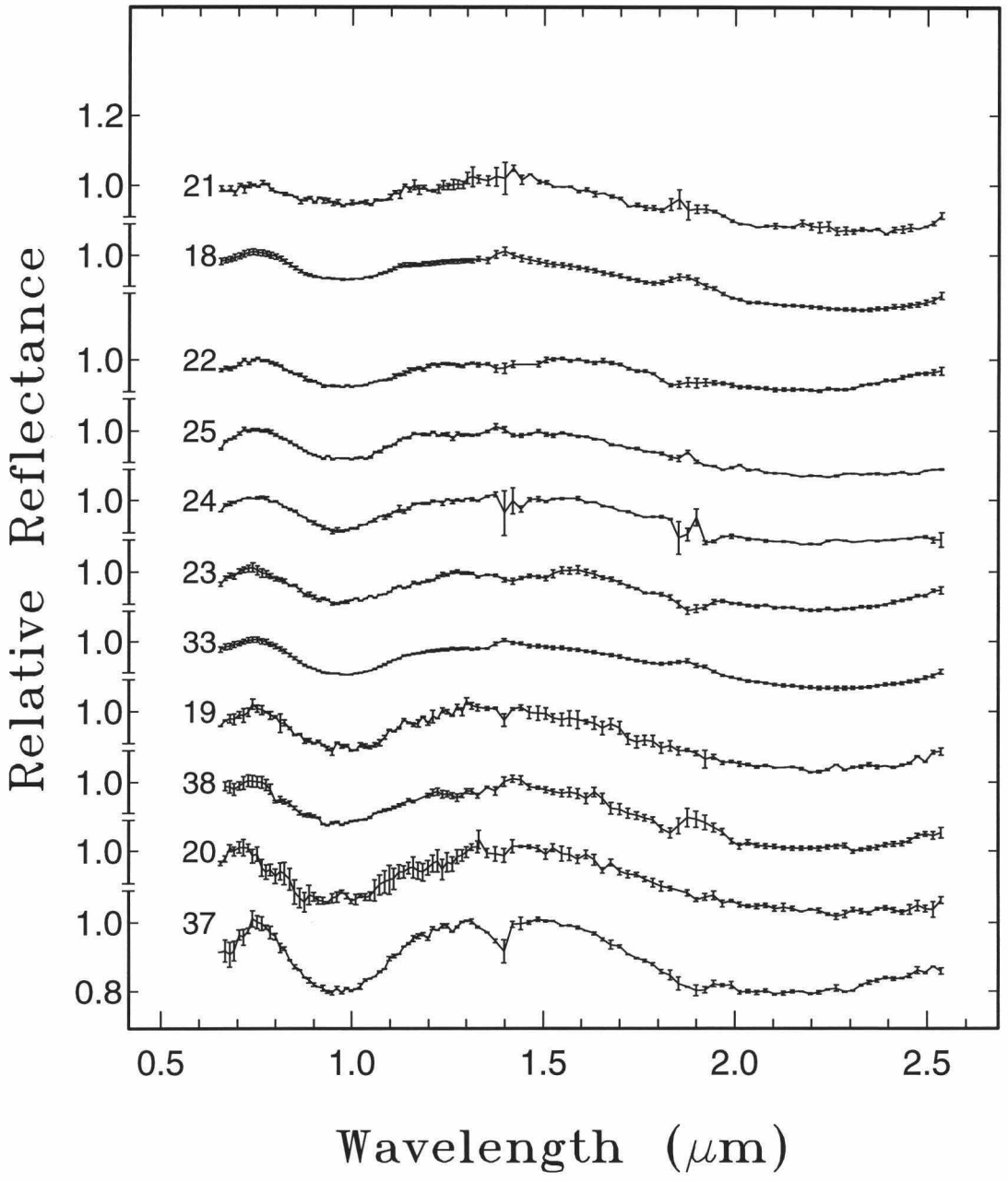

Figure 2.5 (b). Continuum-removed versions of the spectra shown in Figure 2.5 (a).

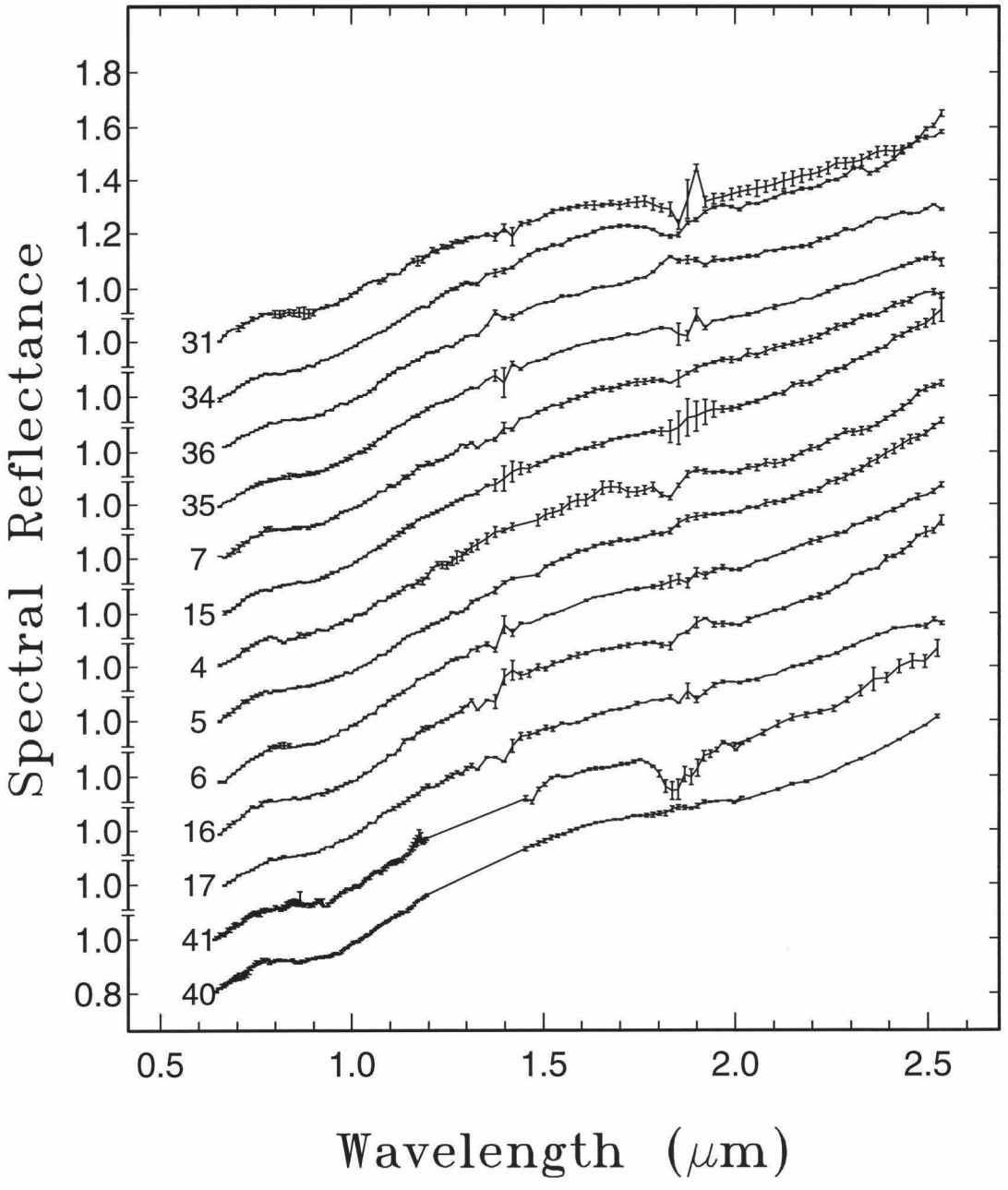

Figure 2.6 (a). Near-IR reflectance spectra (spectra/Sun, scaled to 1.0 at 1.02 μm) for some of the locations given in Figure 1.4 and listed in Table 2.1.

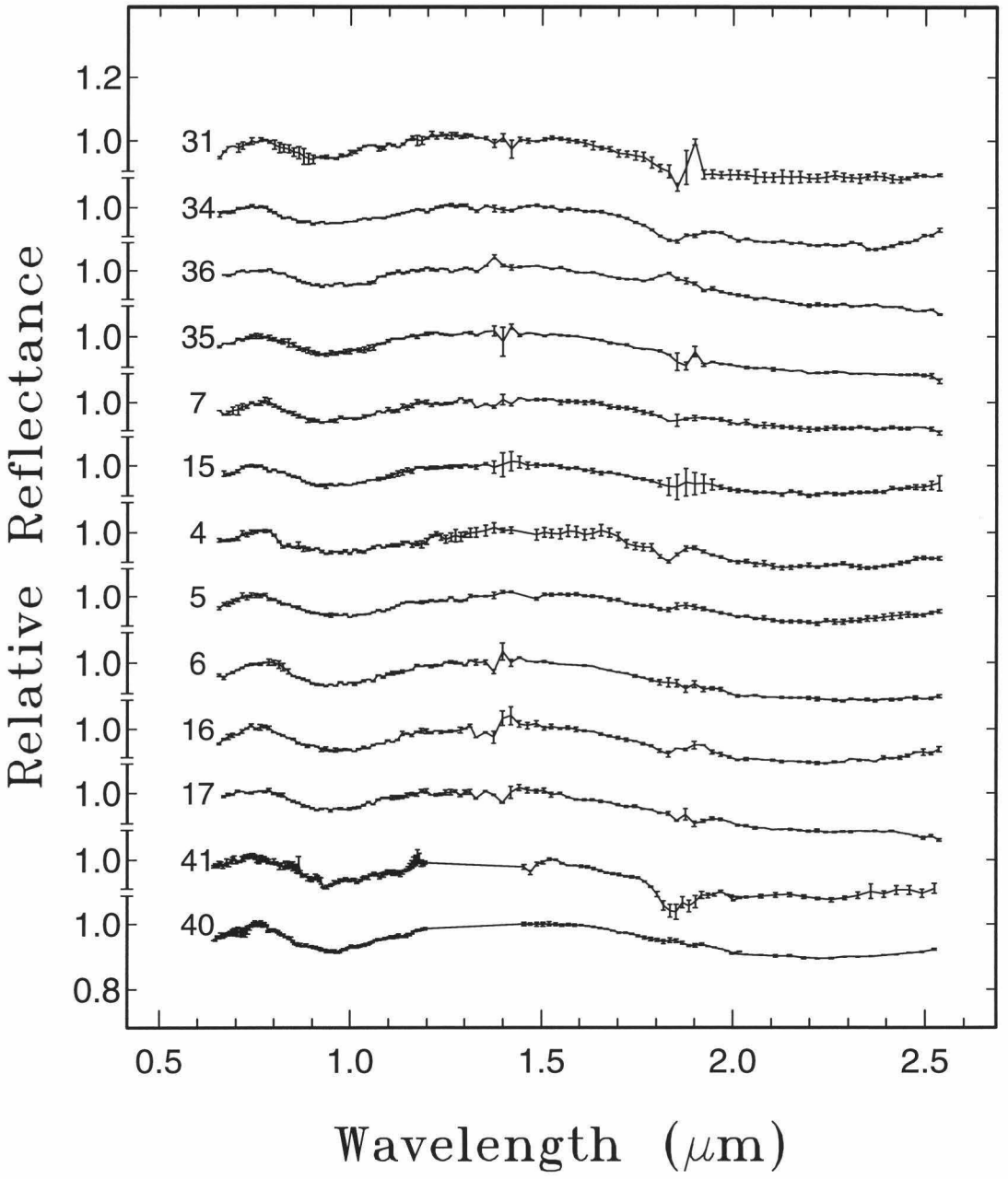

Figure 2.6 (b). Continuum-removed versions of the spectra shown in Figure 2.6 (a).

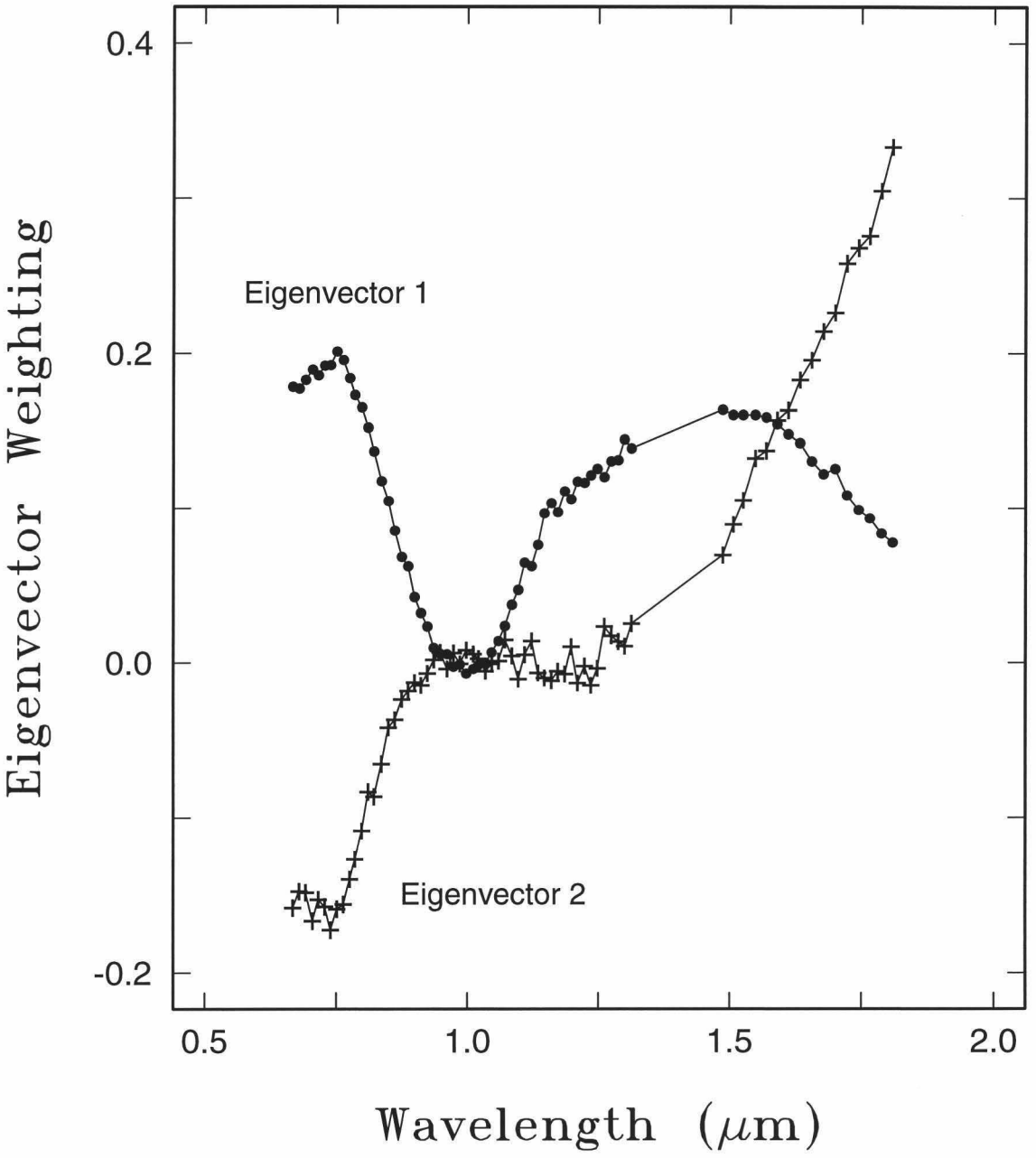

Figure 2.7. First two eigenvectors computed from PCA of Schiller-Schickard spectra.

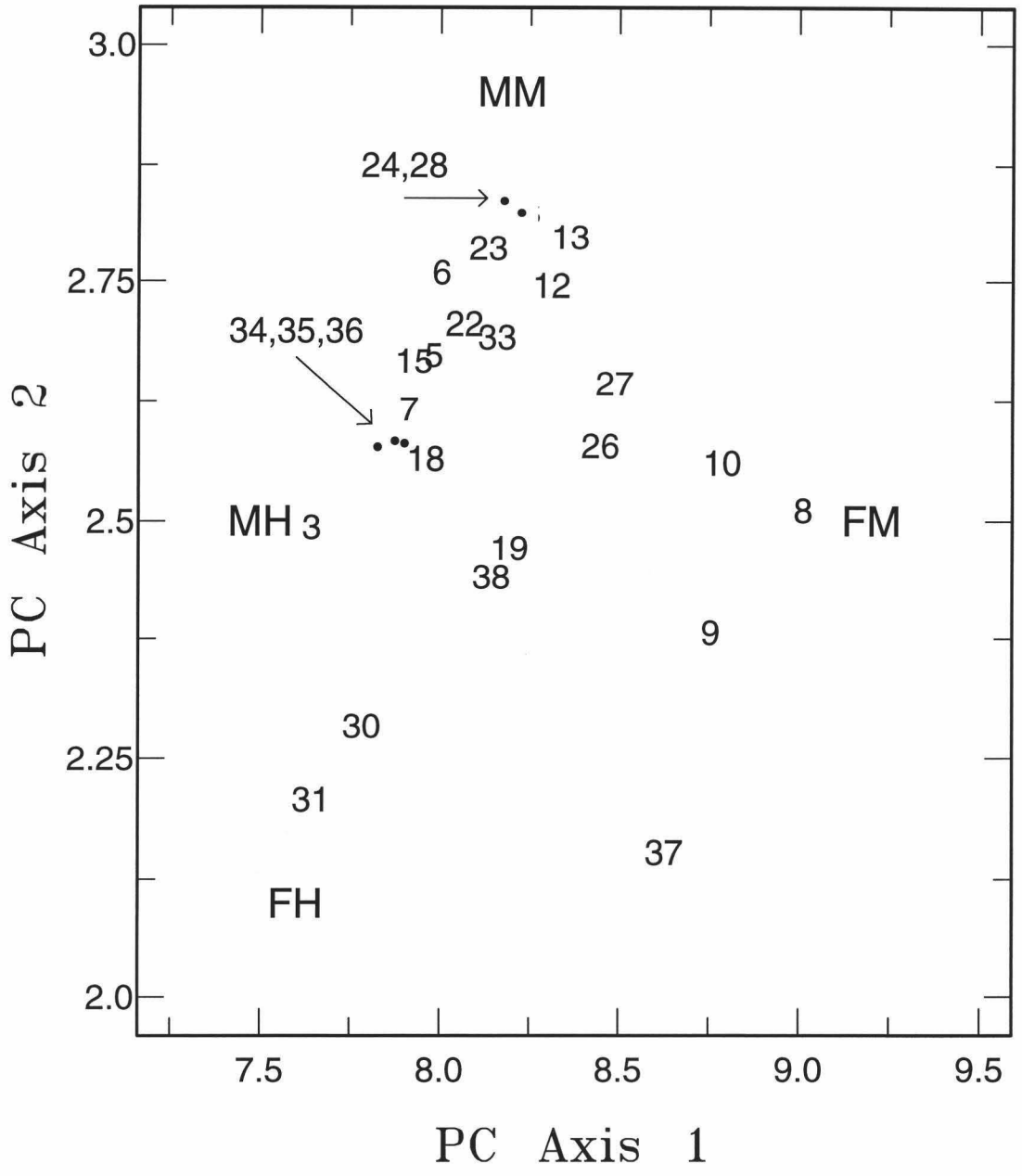

Figure 2.8. Schiller-Schickard spectra projected into principal component space. The numbers identify spectra listed in Table 2.1. Four plausible spectral endmembers were included in the PCA, and these plot near the extremes of a four-sided figure. The endmembers are indicated by MM (mature mare), FM (fresh mare), MH (mature highlands), and FH (fresh highlands).

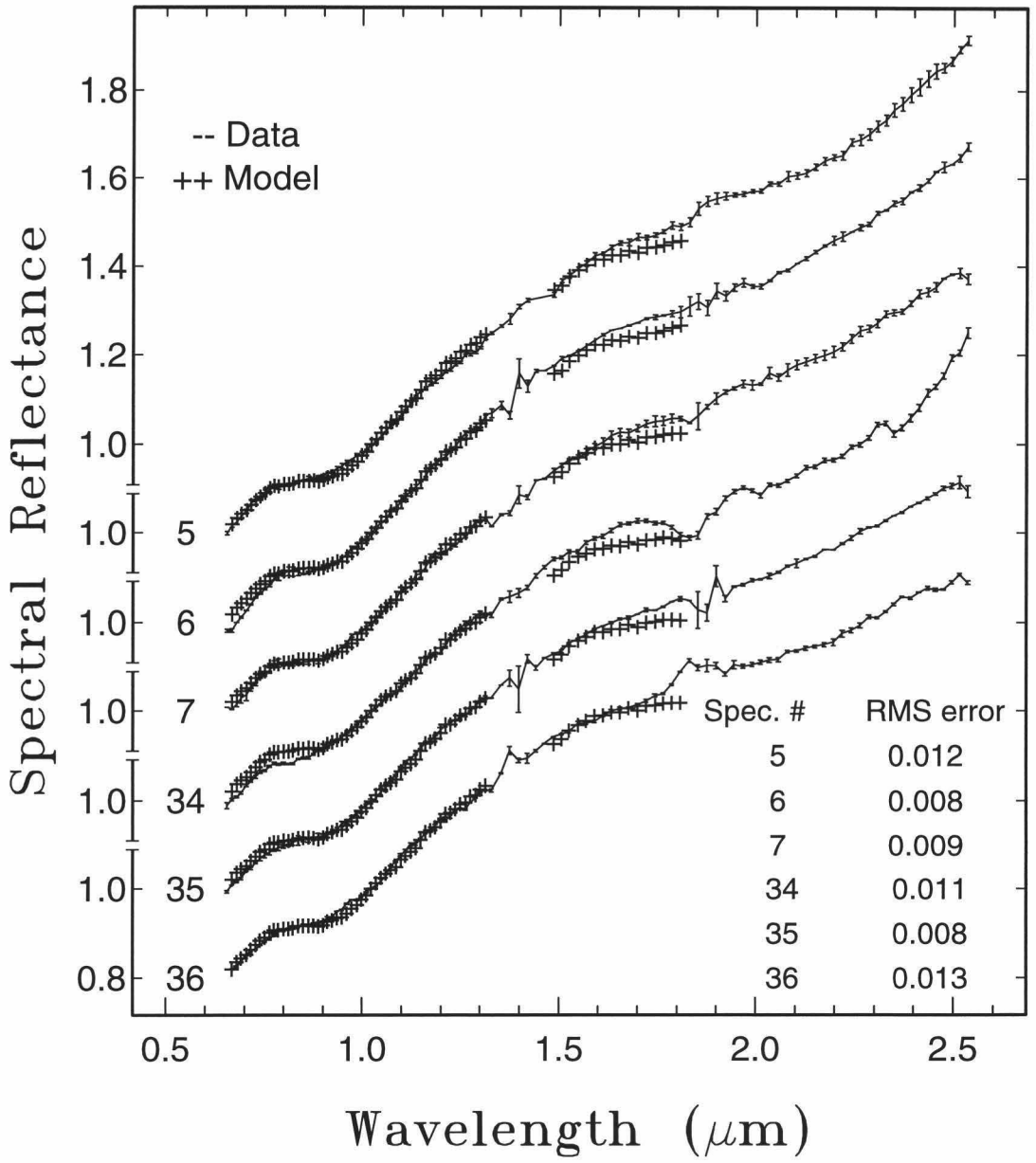

Figure 2.9. Comparison of telescopic spectra with model spectra calculated from two-component PCA mixing analysis. The numbers on the left identify spectral locations given in Table 2.1. Overall error of the model fit is shown in the lower right. The model fits are good in the area of the important "1 μm" mafic mineral absorption band. Portions of the original spectra near atmospheric water absorptions (1.4 and 1.9 μm) and longward of 2.0 μm (thermal contamination) were not included in the analysis.

CHAPTER 3
ANALYSIS OF MULTISPECTRAL IMAGES

3.1 Introduction

The near-infrared reflectance spectra described in Chapter 2 are of high spectral resolution, enabling detailed mineralogical information to be extracted. However, they are of limited spatial extent. In order to gain increased areal coverage, multispectral images may be employed. A previous study has used data from the *Galileo* spacecraft's solid state imaging (SSI) system obtained during the first Earth-Moon encounter to investigate the abundance of mare basalt in the area of the Schickard cryptomare [*Head et al.*, 1993a]. Analysis by the *Galileo* team has focused on imagery in five colors between 0.41 and 0.99 μm, at spatial resolution ranging from ~3.9 to 29.0 km/pixel [*McEwen et al.*, 1993]. Presented here are results based on analysis of Earth-based telescopic multispectral images covering about the same wavelength range, but sampled at a higher spectral resolution (12 colors). Additionally, the spatial resolution of the telescopic images, ~2 km/pixel, is higher than that of the SSI data.

3.2 Image Processing and Analysis

Two multispectral scenes of the SS region (Figure 3.1) were acquired as part of an imaging survey of the Moon carried out with a charge-coupled device (CCD) array camera attached to the 61 cm (Air Force) telescope on Mauna Kea [*Neukum et al.*, 1991]. The first scene (labeled "p4" at the time the data was acquired) covers the southwestern limb of the Moon and includes the northern mare deposit in Schickard and part of the light plains unit on that crater's floor. Scene two ("p5"), to the east of "p4", contains the southern mare unit in Schickard, the Schiller-Zucchius plains, and Schiller crater. Images were obtained in twelve filters, each with a 20 nm bandwidth, centered at the following wavelengths: 0.4, 0.5, 0.55, 0.6, 0.65, 0.72, 0.79, 0.85, 0.89, 0.93, 0.96

and 0.99 μm. Corrections for extinction, dark current, and flat-field were applied, and images were normalized to a standard exposure time [*Neukum et al.*, 1991]. Images with this degree of calibration (differing from absolute reflectance only by additive bias and linear gain factors) are satisfactory for deconvolution with linear mixing models, as discussed further below. Two image cubes (two spatial dimensions, one spectral dimension) were assembled by registering the two sets of 12 filter images with the SUBPREG routine in the PICS image processing system. The 0.72 μm image, acquired in the middle of the filter sequence, was used as the base to which the other filters were registered. Because of large filter-to-filter variations in average DN (digital number) value, the cubes were normalized by dividing by the 12-point spectrum extracted from an area on the north mare patch on the floor of Schickard. This prevented filter images with higher average DN from overly influencing the mixing model fit, and produced results with smaller residual error than the unnormalized cubes. Next, the two 0.72 μm base images were registered to the U. S. Geological Survey digital shaded relief ("airbrush") map of the Moon and placed into an orthographic projection (Figure 3.1).

In order to examine the occurrence and distribution of spectral types, a linear mixing analysis was conducted. Image mixing model calculations were executed with a routine in the SIPS image processing system [*Kruse et al.*, 1993]. The program found the best fit endmember fractions for each pixel subject to the constraints that the individual endmember abundances were ≥ 0 and the sum of the abundances were ≤ 1, such that the RMS difference between the data and model spectra was minimum. Linear mixing was assumed. Linear models provide good first order results and do not require the data to be of high photometric accuracy, as do intimate mixture models.

The number and location of potential endmembers were tested and refined. Four endmember spectral types were finally selected as the average of small areas within the scenes. The endmembers were: 1) mature highlands - an area on the limb highlands

free of bright craters, 2) fresh highlands - bowl and wall material of crater Inghirami C, 3) mature mare - an area of the north mare unit on the floor of Schickard crater, and 4) fresh mare - bowl of Nöggerath F crater. The pixel locations of the endmembers are given in Table 3.1, and the endmember spectra are shown in Figure 3.2. Both image cubes were unmixed using the four endmembers. Constraint violations occurred in a small number of pixels (<1.5% of the total), mostly because of small craters that are brighter than the selected endmembers. The analysis produced an abundance image for each of the endmembers, an image depicting the sum of the endmember fractions, and an RMS error image. The endmember abundance and error images were mosaicked together and reprojected to match the 0.72 μm image (Figures 3.3 - 3.7). Typical RMS errors (excluding bright craters) in the areas of interest around Schiller and Schickard were 9 DN (Figure 3.7). The range of DN in the data images was ~1000-2300, hence the RMS error is <1%.

Table 3.1 Location of Image Endmembers

Endmember Name	Image Cube	Number of pixels averaged	Approximate Location*
mature highlands	p4	17	96,6
fresh highlands	p4	8	256,70
mature mare	p4	11	254,215
fresh mare	p5	5	364,88

*Line and sample coordinates

The most instructive endmember image for consideration here is the mature mare image. To aid in the interpretation of the image, it was density-sliced to 25% increments, as shown in Figure 3.8. The image reveals that significant amounts of mare basalt occur in the surface units in and around Schickard and the terrain to the east, including the Schiller-Zucchius plains and the area surrounding Schiller crater. Elevated mare abundances are found outside of the readily identifiable low albedo mare

deposits. West of Schickard, the limb highlands are mostly free of a mare component. The light plains on the floor of Schickard stand out with proportions of mare basalt mostly in the range 25-75%; the average total mare fraction (fresh+mature) in light plains pixels is ~45%. These findings are in good agreement with those of the mixing model studies utilizing near-IR spectra (Table 2.3, chapter 2), which indicated the presence of ~40-67% mare basalt in the surfaces of several isolated areas on the Schickard light plains unit. It is interesting to note that the average total mare basalt abundance in Schickard light plains pixels as determined from the multispectral images (45%) is in excellent agreement with the amounts of mare material (44-46%) present in the ejecta of the 1.4 km light plains crater as determined by mixing model analysis of near-IR spectra.

The light plains on the floor of Schiller crater have an average mature mare abundance of about 40%, though small areas on the north central part of the floor where the near-IR spectrum was obtained exhibit mare fractions approaching 60%. The spectral mixing model described in section 2.4.4 of Chapter 2 found 70% basalt for the Schiller floor spectrum.

High mare basalt abundances also exist in the vicinity of the DHC's Drebbel F and Nöggerath F, and the post-Orientale Schiller-Zucchius plains are shown to be dominated by mare basalt (Figures 3.3 and 3.8). Portions of the Schiller-Zucchius plains display mare fractions >75%; this is in accordance with the results from the spectra which suggested ~85% mare component. The present findings are in good agreement with those reported by *Mustard et al.* [1992] and *Head et al.* [1993a].

3.3 Discussion

The mixing model results shown in Figure 3.8 clearly indicate that the highlands units in the Schiller-Schickard region generally contain large amounts of mare basalt.

The modeled percentages generally range between 25% and 75%. The results for the light plains in Schiller crater and Schickard crater were discussed above, but numerous other light plains deposits occur in the region and these also exhibit relatively high abundances of mare material. In a few areas, the amounts of mare debris in the light plains exceeds 75%, but areas with 50-75% are much more common. It is important to note that large expanses of non-plains highlands terrain in the SS region also exhibit abundances of mare basalt that range between 25% and 75%.

One possible explanation for the large amounts of mare basalt associated with the light plains units in the SS region is that pure highlands debris was emplaced on top of pre-existing mare units as a consequence of the Orientale impact event, and that mare material was excavated and added to the regolith by subsequent impact cratering events. Is this vertical mixing scenario viable? The bulk of the evidence suggests that it is not. First, evidence was presented in section 2.4.4 that the subsurface portion of the light plains unit in the floor of Schickard crater contains ~45% mare material, based on spectral analysis of the fresh 1.4 km diameter crater. If vertical mixing was responsible for the high percentage of mare material associated within the SS light plains, one would expect that this mare component would be concentrated in the near-surface layer and absent in the interior of the plains unit. This is not true for the light plains on the floor of Schickard. Second, the distribution of mare-rich material in the region argues against the vertical mixing hypothesis. As shown in Figure 3.8 most highlands units in the SS region exhibit mare abundances in excess of 25%. The enhanced mare abundances are not confined to the light plains; they also occur in elevated and relatively rugged areas that were unlikely to have been the site of pre-Orientale volcanism. Additional evidence was presented by *Pieters et al.* [1993]. They noted that SSI spectrum 74 has a very strong ferrous absorption band at ~1 μm and that its spectral properties indicate the presence of a large amount of freshly exposed mare basalt. This

SSI spectrum was derived for a small, fresh crater on a highlands ridge between the craters Nasmyth and Phocylides. It is unlikely that mare basalts were erupted on this ridge after the formation of Nasmyth and Phocylides. A more probable explanation is that ancient mare basalts were disrupted by Orientale secondary-forming projectiles and incorporated into a debris flow which moved radially away from Orientale and deposited mare-rich material on the ridge. This process appears to offer the best explanation for the presence of an abundant mare component in other elevated and rugged terrain downrange from light plains units that display dark-haloed impact craters.

The origin of the light plains on the floor of Schiller is uncertain. As discussed above, these plains possess an average mare abundance of almost 40%. *Greeley et al.* [1993] presented crater statistics that yielded a model age of 3.73 Ga for the Schiller floor light plains. If this age is correct, mare basalt was extruded on the floor of Schiller at ~3.73 Ga and subsequently contaminated by highlands lithologies emplaced by vertical mixing and lateral transport processes. The prime candidate for supplying such highlands contamination is the nearby Copernican-age crater Zucchius. However, the post-Orientale Schiller-Zucchius plains, which lie closer to Zucchius crater and exhibit obvious Zucchius rays and secondary craters, are less contaminated with highlands material (*cf.* Section 2.4.5).

Another possibility exists for the origin of the light plains on the floor of Schiller. According to the alternate hypothesis, these plains were emplaced as a consequence of the Orientale impact event, and the mare component results from the excavation of pre-existing basalts by Orientale secondaries and the incorporation of this mare material into the radial-flowing debris surge that moved across the interior of Schiller. This hypothesis does not account for the crater model age, though the uncertainties of the

crater statistics may make 3.73 Ga indistinguishable from the 3.84 age of Orientale. Additional information will be required to resolve this issue.

Finally, it should be noted that enhanced mare basalt abundances exist in the highlands terrain surrounding Lacus Excellentiae and other mare units south of Mare Humorum. This area can be seen in the upper portion of Figures 3.3 and 3.8. Mare abundances of 25-50% are common in light plains and other highlands units in this area. Similar enhancements can also bee seen in the mare abundance images presented by *Mustard et al.* [1992] and *Head et al.* [1993a]. It seems likely that cryptomaria are present in this area. The emplacement of ancient, pre-Orientale mare basalts in this region may have been facilitated by the presence of a topographic depression within a large impact structure located between the Humorum basin and the Schiller-Zucchius basin.

Figure 3.1. CCD images of the Schiller-Schickard region made through a 0.72 μm filter. The images have been placed in an orthographic projection centered at (0°, 0°). Compare with Figures 1.2, 1.3, and 1.4.

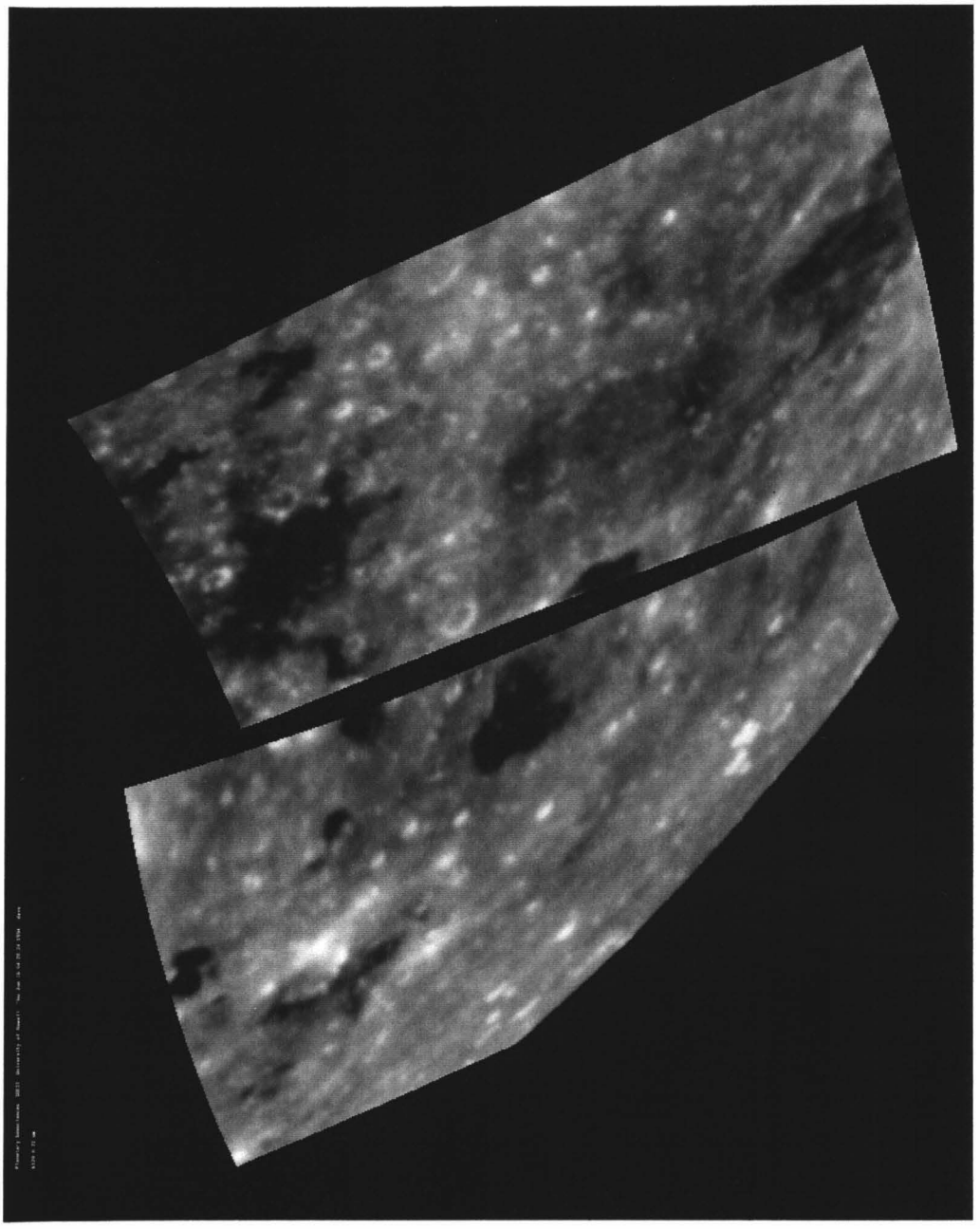

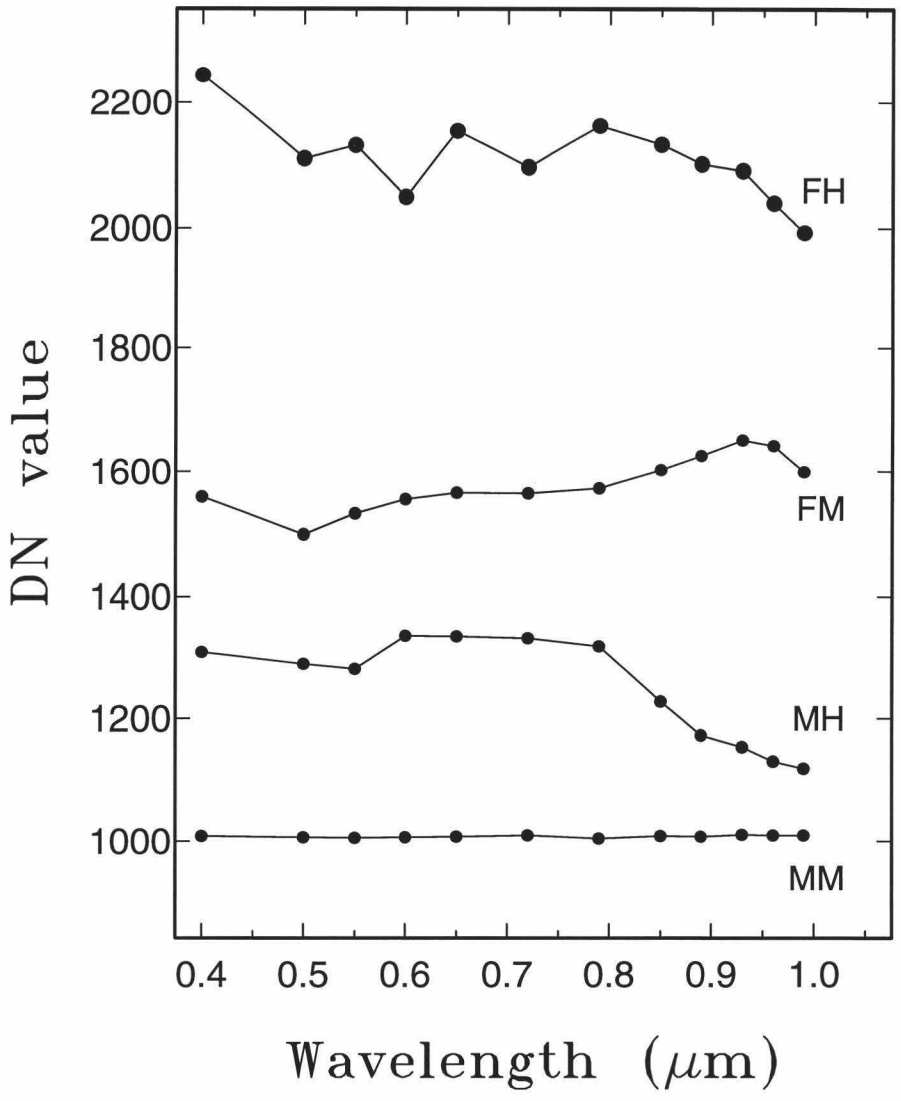

Figure 3.2. Endmember spectra extracted from image cubes. FH = fresh highlands. FM = fresh mare. MH = mature highlands. MM = mature mare.

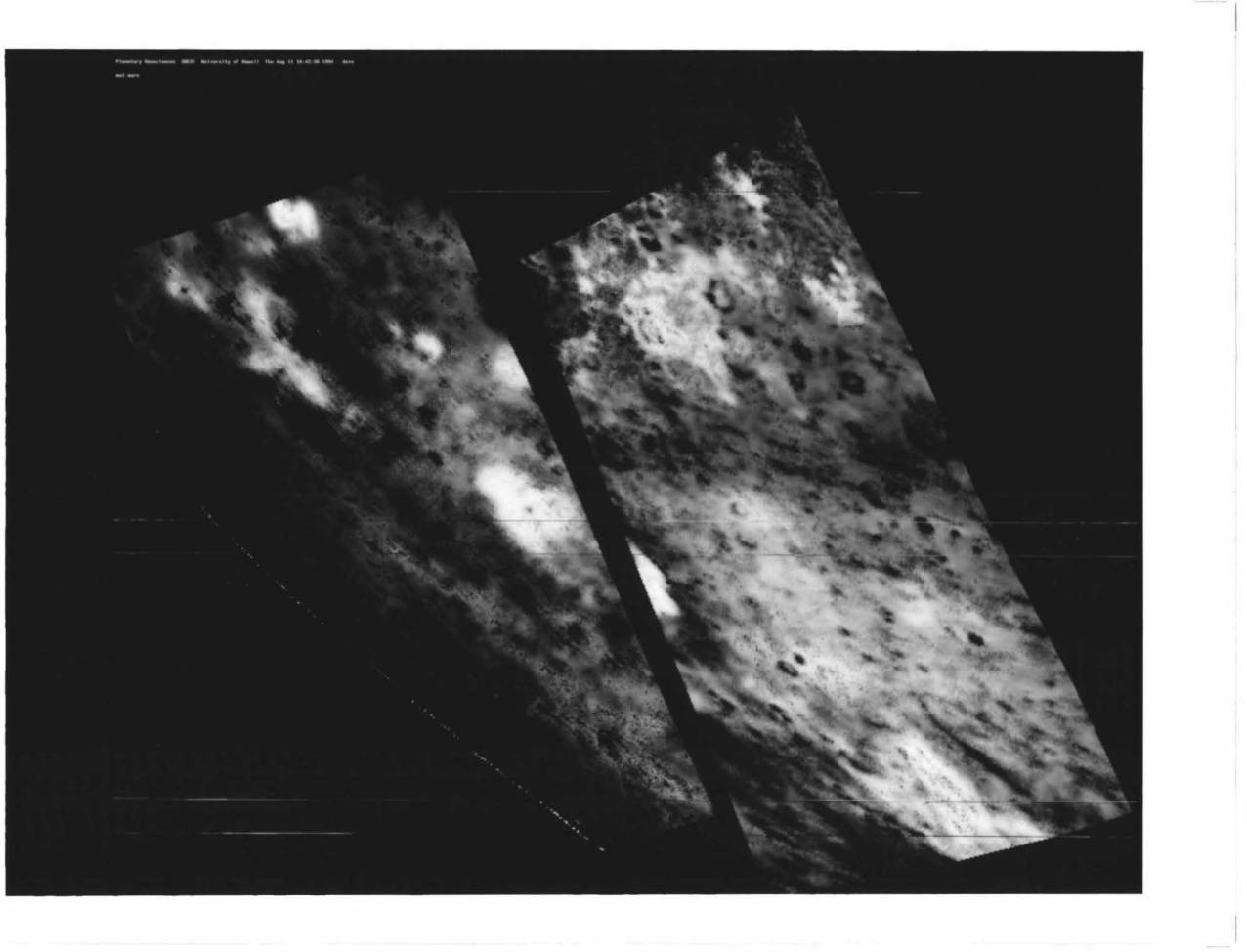

Figure 3.3. Results of image spectral mixing analysis. Shown is the model abundance of the mature mare endmember. Projection is the same as Figure 3.1. Horizontal lines are errors introduced in the process of sending the image to the filmwriter.

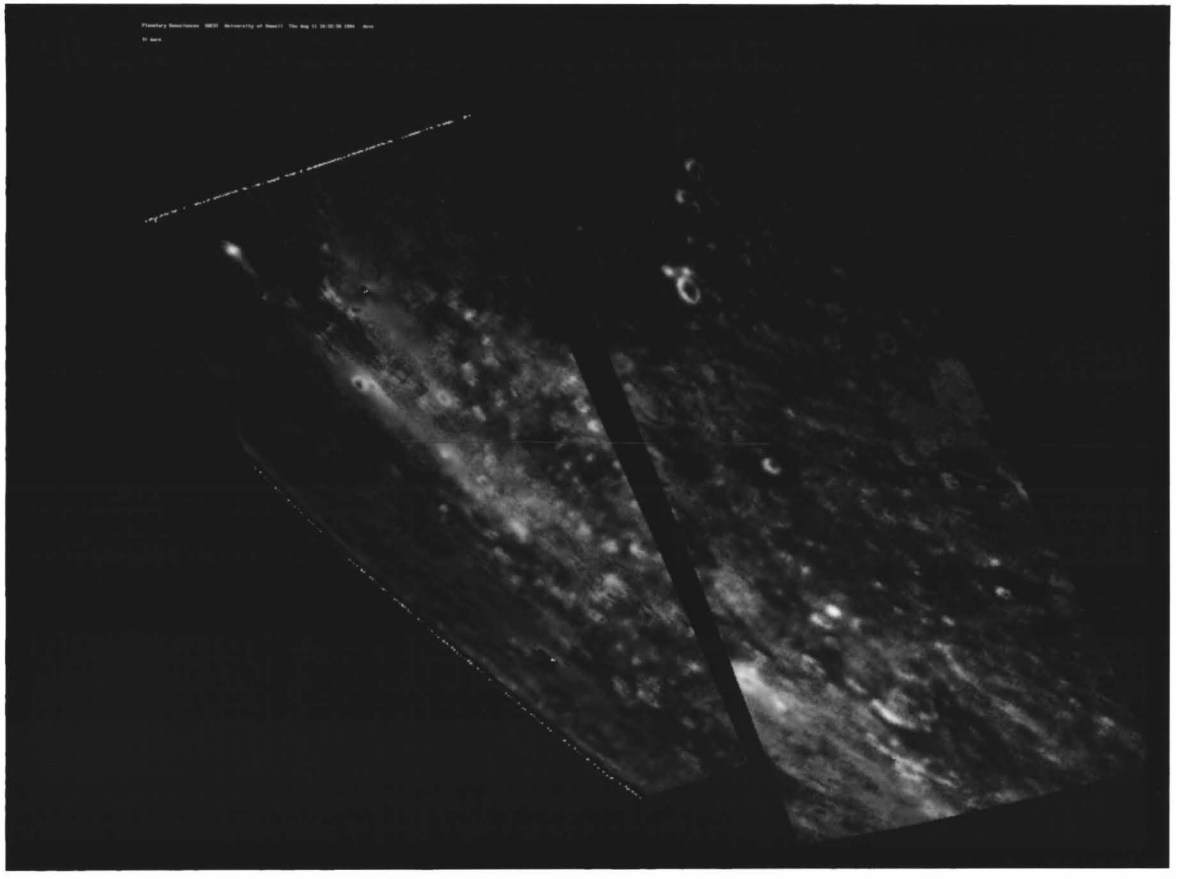

Figure 3.4. Results of image spectral mixing analysis. Shown is the model abundance of the fresh mare endmember. Projection is the same as Figure 3.1. Horizontal line near the middle of the images is an error introduced in the process of sending the image to the filmwriter.

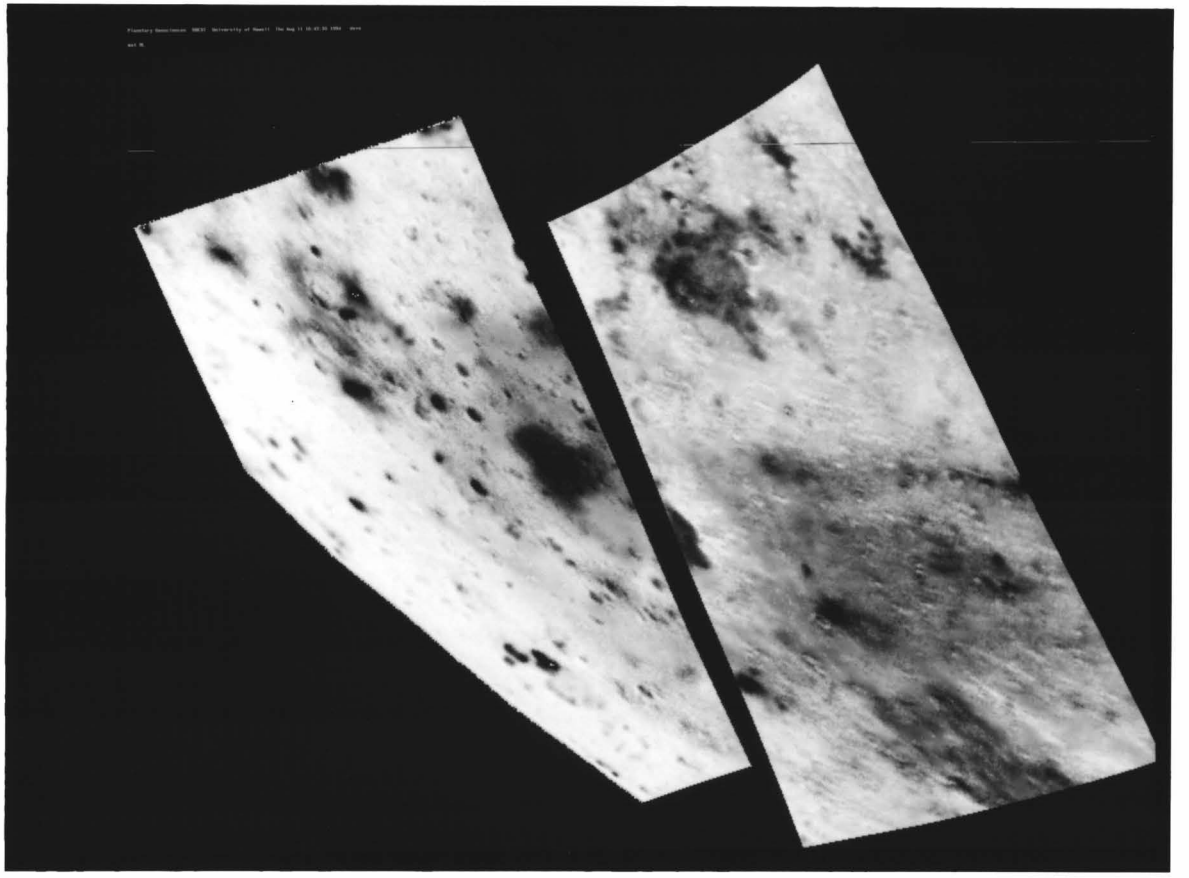

Figure 3.5. Results of image spectral mixing analysis. Shown is the model abundance of the mature highlands endmember. The projection is the same as Figure 3.1. Horizontal line near the top is an error introduced in process of sending the image to the filmwriter.

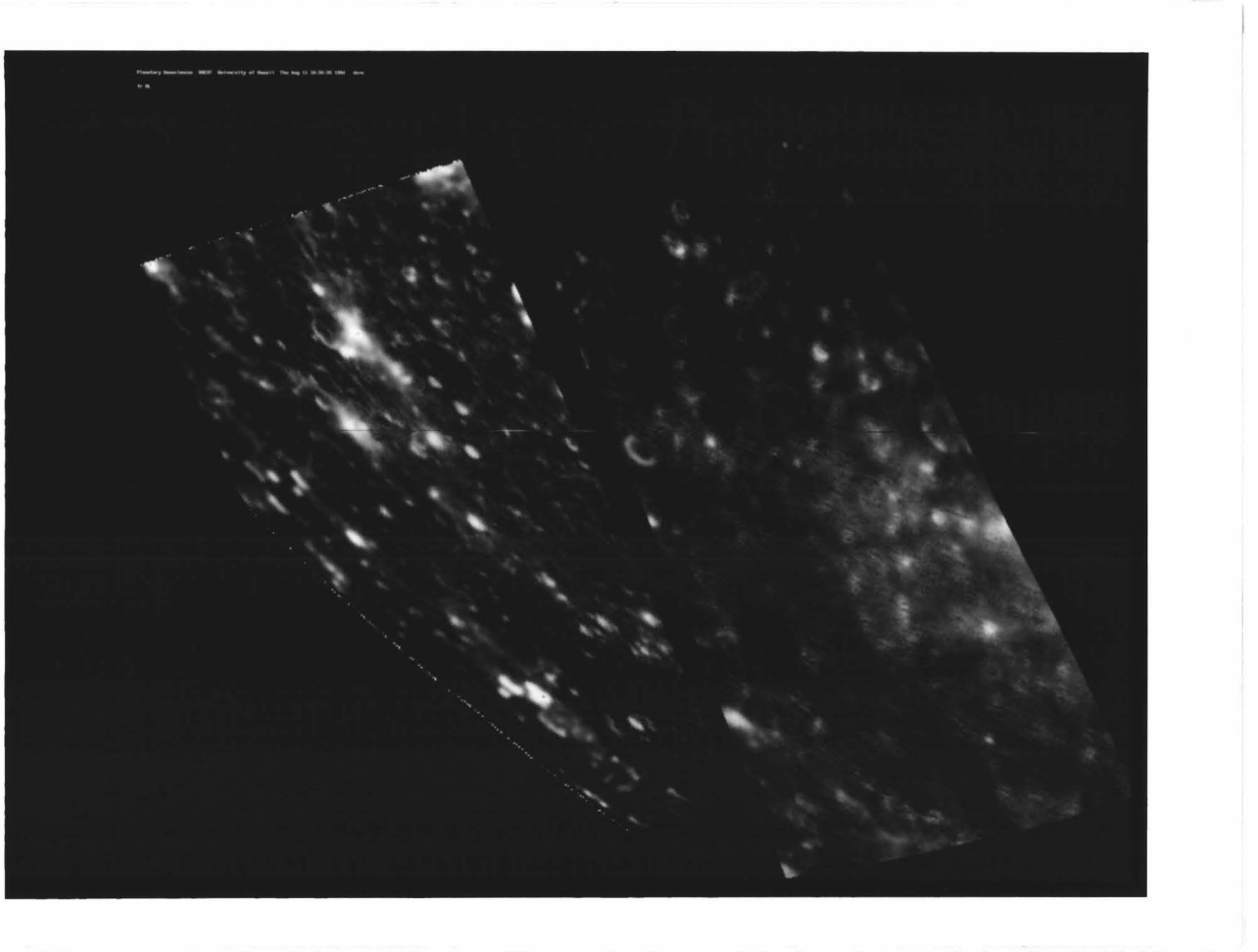

Figure 3.6. Results of image spectral mixing analysis. Shown is the model abundance of the fresh highlands endmember. Projection is the same as Figure 3.1. Horizontal line near the middle is an error introduced in the process of sending the image to the filmwriter.

Figure 3.7. Results of image spectral mixing analysis. Shown is the RMS error between the data image and the calculated model. Projection is the same as Figure 3.1. The stretch is 0-100 DN. This image reveals that the model fits the data very well everywhere except for a few bright craters that were brighter than any of the chosen endmembers.

Figure 3.8. Results of image spectral mixing analysis. Shown is the mature mare abundance (Figure 3.3), density sliced to show 25% increments. Black = 0-25%, dark grey = 26-50%, light grey = 51-75%, white = 76-100% mature mare. The projection is the same as Figure 3.1.

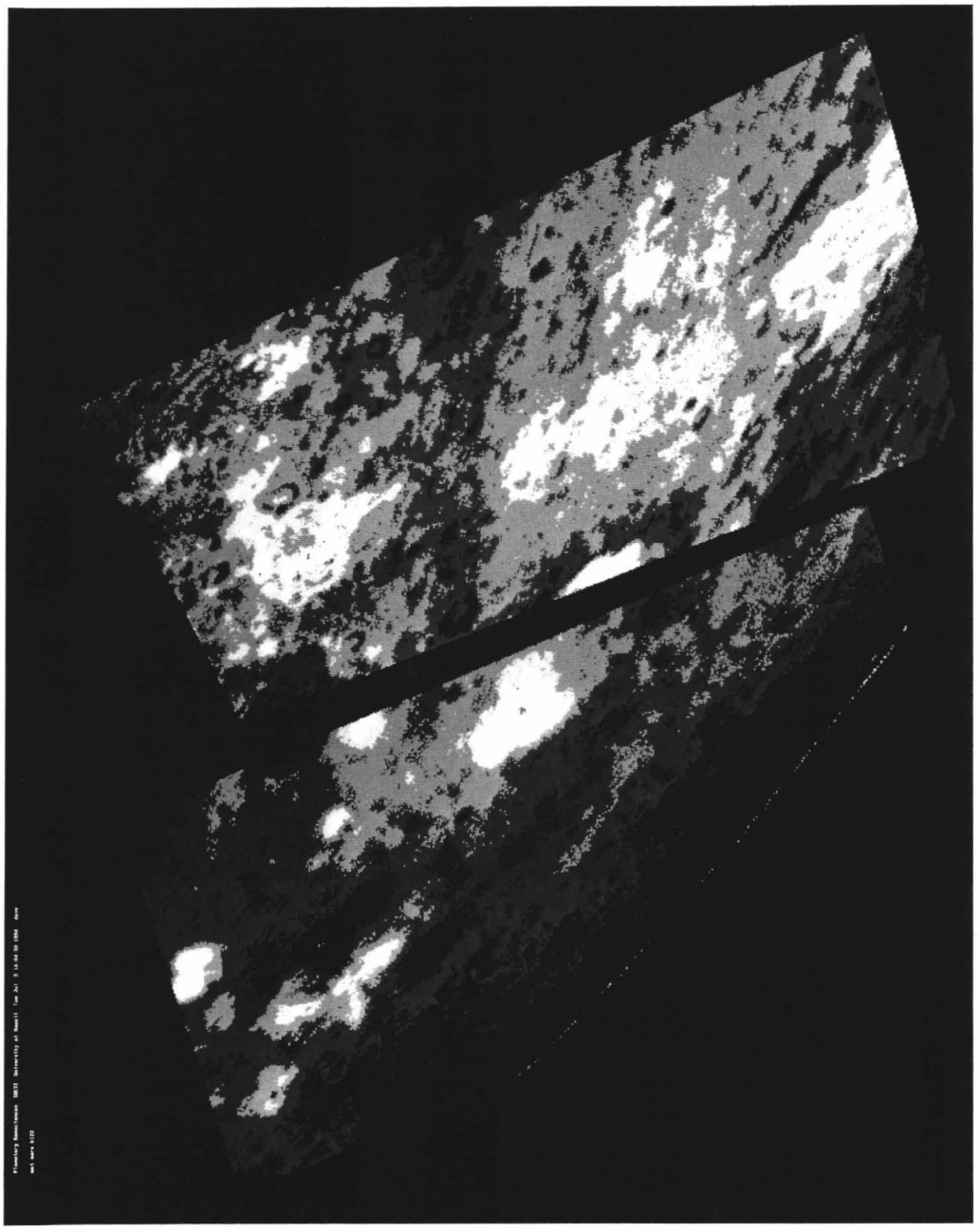

CHAPTER 4
IMPLICATIONS FOR THE LOCAL MIXING HYPOTHESIS

4.1 The Problem Of Basin Ejecta Emplacement

The processes responsible for the emplacement of the distal deposits of lunar impact basins have long been the source of considerable debate. The term "distal deposits" is used here to indicate the outer portions of the ejecta units surrounding large impact structures. Possible modes of emplacement have been discussed in detail by a number of workers [e.g., *Eggleton and Schaber*, 1972; *Chao*, 1974; *Oberbeck*, 1975; *Oberbeck et al.*, 1974, 1975a,b; *Head and Hawke*, 1975; *Hawke and Head*, 1978; *Moore et al.*, 1974; and *Wilhelms*, 1987]. Four major models are illustrated in Figure 4.1. One model (panel A in Figure 4.1) emphasizes the importance of surface flow. According to this hypothesis, basin material is transported for long distances (hundreds of kilometers) as a ground-hugging debris flow. When the flow comes to rest, a layer of primary basin material has been deposited atop local material. The second possible mode of emplacement is shown in panel B of Figure 4.1. In this model, material is excavated from the transient crater and travels in ballistic trajectories to the point of impact and deposition. There is no surface flow and minimal interaction with the substrate. Hence primary basin ejecta is deposited on top of local, non-basin material. Panel C of Figure 4.1 represents a third possible mode of distal basin ejecta emplacement. According to this model, primary basin ejecta is transported for relatively long distances in ballistic flight, and upon re-impact moves as a surface flow for tens of kilometers. There is little or no significant reworking of the pre-impact surface, and when the flow comes to rest a layer of primary basin ejecta lies above the local material. Finally, the ballistic erosion and sedimentation model of Oberbeck and coworkers is depicted in panel D of Figure 4.1.

The model of Oberbeck and coworkers [*Oberbeck et al.*, 1974, 1975a,b; *Oberbeck*, 1975; *Morrison and Oberbeck*, 1975], which has become known as the ballistic erosion and sedimentation or local mixing hypothesis, considers secondary cratering to be a major process in modifying and redistributing material on the lunar surface. In the Oberbeck model, the velocity component of the secondary crater ejecta radial to the primary gives rise to a debris surge which moves outward behind the ejecta curtain. At large distances from the primary, the mass ejected from the secondary craters can exceed the mass of the primary ejecta projectiles that formed them. Thus the debris surge entrains material of both primary and local origin, with local material dominating the distal deposits. The ejecta curtain and debris surge are similar to the two regimes of transport envisioned by *Eggleton and Schaber* [1972]: one ballistic and the other highly fluidized and able to flow over obstacles and pool in depressions. However, *Eggleton and Schaber* [1972] postulated a fluidizing medium of melted or vaporized rock, and also considered the deposits to consist predominately of primary ejecta.

4.2 Testing the Ballistic Erosion Model

Oberbeck et al. [1975a] developed relationships to calculate the degree of local mixing produced by secondary cratering as a function of the size of the secondary craters formed, the angle at which the secondary-forming projectiles strike the surface, and the distance from the primary impact. The key equation is (Eqn. 2 of *Oberbeck et al.* [1975a]):

$$\mu = 46.4\left[\frac{\sin 2\theta_s}{2\tan\left(R_s/3472\right)} + \sin^2\theta_s\right]^{-1} D_{rs}^{-0.401}\cos^{1.134}\theta_s, \qquad (4.1)$$

where

μ = ratio of mass ejected from secondary crater to mass of secondary-forming projectile

θ_s = impact angle (measured from the surface normal)

R_s = distance of secondary crater from primary (in kilometers)

D_{rs} = diameter of secondary crater (in kilometers).

The ballistic erosion hypothesis may be tested if there is some available means to distinguish between the primary ejecta and the substrate with which the ejecta interacts; this is not often the case. The rays of Copernicus crater, which were formed by the interaction of highlands-rich primary ejecta with local mare basalt, were the subject of a previous attempt to evaluate the local mixing model [*Pieters et al.*, 1985]. The study found that the proportion of mare to highlands spectral types in the rays was consistent with the Oberbeck prediction. The light plains deposits in the Schiller-Schickard region offer a rare opportunity to determine the relative amounts of primary ejecta and secondary crater ejecta (i.e., local material) in the distal deposits of a basin-size impact. This is so because the composition of Orientale primary material is very different from the substrate (mare basalt) present in large portions of the Schiller-Schickard region at the time of the Orientale impact event [*Hawke et al.*, 1991; *Head et al.*, 1993b]. Hence it is possible to test the local mixing hypothesis for the origin of the distal deposits of the Orientale basin.

In order to apply the Oberbeck equation, Orientale secondary craters in and near Schickard were identified on Lunar Orbiter IV photographs with the aid of the map by *Karlstrom* [1974], and the diameters measured. A range of values was found, from a few kilometers for craters found in small groups, to as a much as 14 km for some isolated secondaries. The radial distance from the ejection point within the primary impact to the secondary crater cannot be exactly determined, so an average distance was used equal to the distance from the transient cavity rim to the secondary, plus one-half

of the transient cavity radius. For Orientale, the transient cavity rim was taken to be the Outer Rook mountains [*Head*, 1974]. The great circle distance from the Outer Rooks to the center of Schickard crater is approximately 958 km. The diameter of the Outer Rook ring is 620 km [*Wilhelms*, 1987], so the distance R_s used in the Oberbeck equation was 958 + (620)/4 = 1113 km. The Oberbeck equation is not strongly dependent on the radial distance, and variations of plus or minus 100 km in R_s (representing slight differences in the distance to the individual measured secondaries) do not cause substantial changes in the outcome of the calculation. The impact angle was taken to be 75° from the vertical, the value favored by *Oberbeck et al.* [1975a] based on studies of the secondary craters of Copernicus. (Smaller impact angles result in greater secondary cratering efficiencies because more of the energy of the secondary-forming projectile is directed into the target, and less energy is directed down-range. Similarly, impact angles >75° produce less local mixing.) Equation 4.1 expresses the degree of local mixing as a ratio μ, equal to the mass of the excavated local material divided by the mass of the secondary-forming projectile. The proportion of local material is therefore given by $\mu/(\mu+1)$, and this quantity has been plotted in Figure 4.2. Also shown is a curve given by the original Oberbeck relation modified by a change in the assumed impact scaling law, as suggested by H. J. Moore (quoted by *Wilhelms* [1987], p. 211). The modified relation has the initial factor equal to 30.5 (instead of 46.4), the exponent of D_{rs} is -0.6, and the exponent of the cosine term is 1.2.

The plotted values in Figure 4.2 indicate that for the secondary crater sizes encountered near Schickard, the expected fraction of local material ranges from about 40-80%. The remote sensing data presented in the previous section indicate that the amount of mare basalt contained in the Schickard light plains is generally 40-67%, with an average of about 45%. The abundances of mare basalt were also determined for two extensive clusters of Orientale secondary craters located adjacent to the Schiller-

Zucchius plains southeast of Schickard (Figure 1.1). The northern cluster (centered approximately at 47° W, 51.7° S) contains craters that range from a few kilometers to 8 km in diameter. The southern cluster (~47° W, 55.5° S) has larger craters that are 5 to 15 km in diameter. Calculations made according to the methods described above indicate that the amounts of local material associated with the northern cluster should range between 45% and 85%. The calculated fractions of local material in the southern cluster are between 42% and 82%. The results of our image mixing model analysis indicate that the material associated with the secondary crater clusters in the Schiller-Zucchius area is dominated by mare debris. The abundances of mare basalt generally range between 50% and 75% (Figure 3.3). Therefore, the extent to which local material was incorporated into the distal deposits of the Orientale basin by secondary craters is in general accord with the predictions of the ballistic erosion model.

While the validity of the local mixing hypothesis has been demonstrated, it should be noted that the amounts of local material present in the distal deposits of Orientale are rarely equal to the maximum values predicted by the original Oberbeck equation. A number of factors could contribute to a decreased proportion of local material. The first set of factors is related to the assumptions underlying the ballistic erosion model as presented by Oberbeck and co-workers. In some areas, the remote sensing results match the predictions of the modified Oberbeck relation more closely than those of the equation in its original form. Therefore the scaling relation between crater diameter and impact energy of the modified model may be more nearly correct. In addition, *Schultz and Gault* [1985] have emphasized that secondary craters are likely to be formed by fragmented projectiles. They performed laboratory scale impact studies which demonstrate that disrupted impactors displace less target material than do single-body impactors. Therefore the Oberbeck relation, which was developed using assumptions

from the study of laboratory and explosion analogs of single-body impacts, could overestimate the cratering efficiency of secondaries.

However, there are geological factors that could also account for abundances of mare basalt less than the maximum values predicted by the original Oberbeck relation. Chief among these is contamination of Orientale-related deposits by highlands materials from nearby impacts in the time since the Orientale basin-forming event. While this effect is probably minor for the light plains on the floor of Schickard crater, it is important for the Orientale secondaries adjacent to the Schiller-Zucchius plains. As discussed above, the Schiller-Zucchius plains are a post-Orientale mare deposit. The surfaces of even the darkest portions of this mare unit contain ~15% highlands debris contributed by Zucchius and other post-mare impacts (Section 2.4.5). Hence, it seems likely that the nearby Orientale secondary clusters have been contaminated by at least 15% highlands material from Zucchius and other craters. The southern cluster, which is closer to Zucchius, may have been contaminated by even greater amounts of highlands debris.

The evidence provided by the distribution of DHC's in the SS region was used by *Hawke and Bell* [1981] and *Bell and Hawke* [1984] to argue that the pre-Orientale mare deposits in the area were widespread and discontinuous, similar to the present-day appearance of Mare Australe. The thin, patchy nature of the pre-existing mare units would mean that less basalt was available for incorporation into the deposits resulting from the impact of Orientale primary ejecta. In addition, large Orientale secondary craters (10-15 km in diameter) could have easily excavated highlands material from beneath thin (100's of meters) mare units. Since many portions of the discontinuous pre-Orientale mare deposits appear to be relatively thin, it is not surprising that the larger Orientale secondary-forming projectiles penetrated the mare units and incorporated subjacent highlands debris into the resulting deposit.

In summary, the results of both near-IR spectral studies and a mixing model analysis of multispectral images demonstrate that large amounts of local mare basalt are present in light plains and other distal deposits of the Orientale basin in the Schiller-Schickard region. The local material is present throughout the entire thickness of the light plains. The local mare basalt is not just a surface concentration introduced by vertical mixing from beneath the Orientale ejecta deposit. Orientale secondary-forming projectiles excavated local mare material and incorporated this debris into the resulting deposits. The amounts of local material (pre-Orientale mare basalt) present in the light plains and other units in the SS region emplaced as a consequence of the Orientale impact event approach, but rarely exceed, the maximum values calculated using the original Oberbeck relationship. While the original Oberbeck equation may overestimate the cratering efficiency of secondaries, there are a number of geologic factors that could also account for abundances of local mare materials that are less than the values predicted by Oberbeck. These include the thin, discontinuous nature of the ancient mare units in the SS region, as well as the contamination of Orientale-related deposits by highlands debris emplaced by nearby impacts in the time since the formation of the Orientale basin.

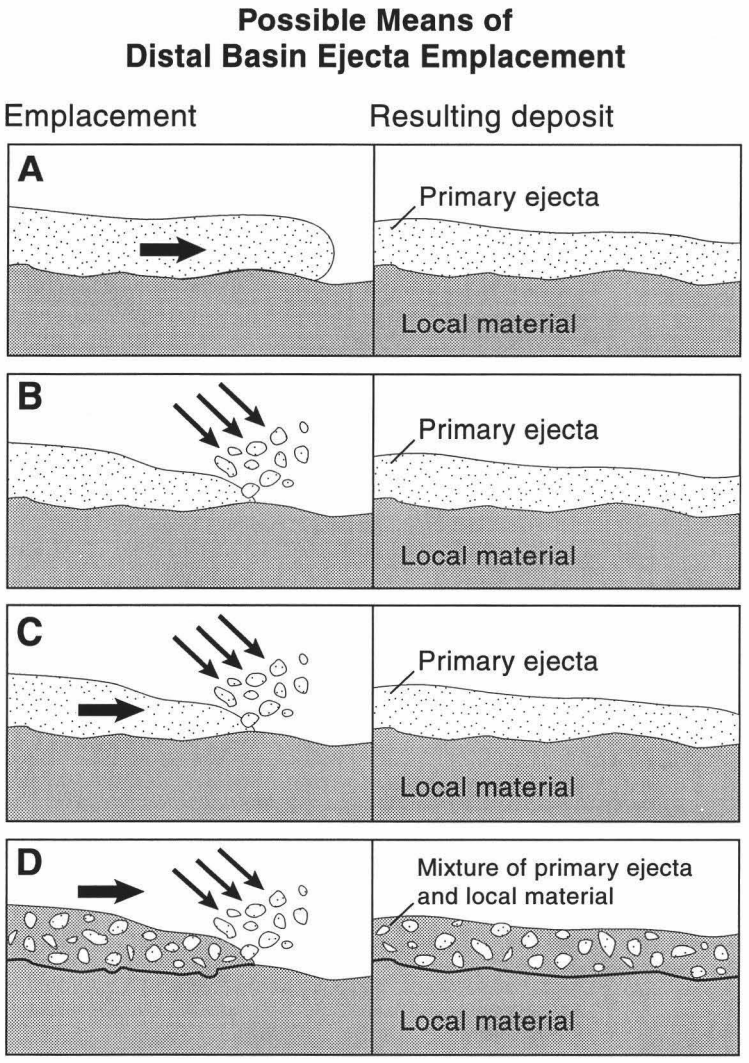

Figure 4.1. Representation of possible modes of basin ejecta emplacement. A. Surface flow. B. Ballistic emplacement. C. Ballistic emplacement induces surface flow. D. Ballistic erosion and sedimentation. For each, the left panel depicts the emplacement process and the right panel shows the resulting deposit.

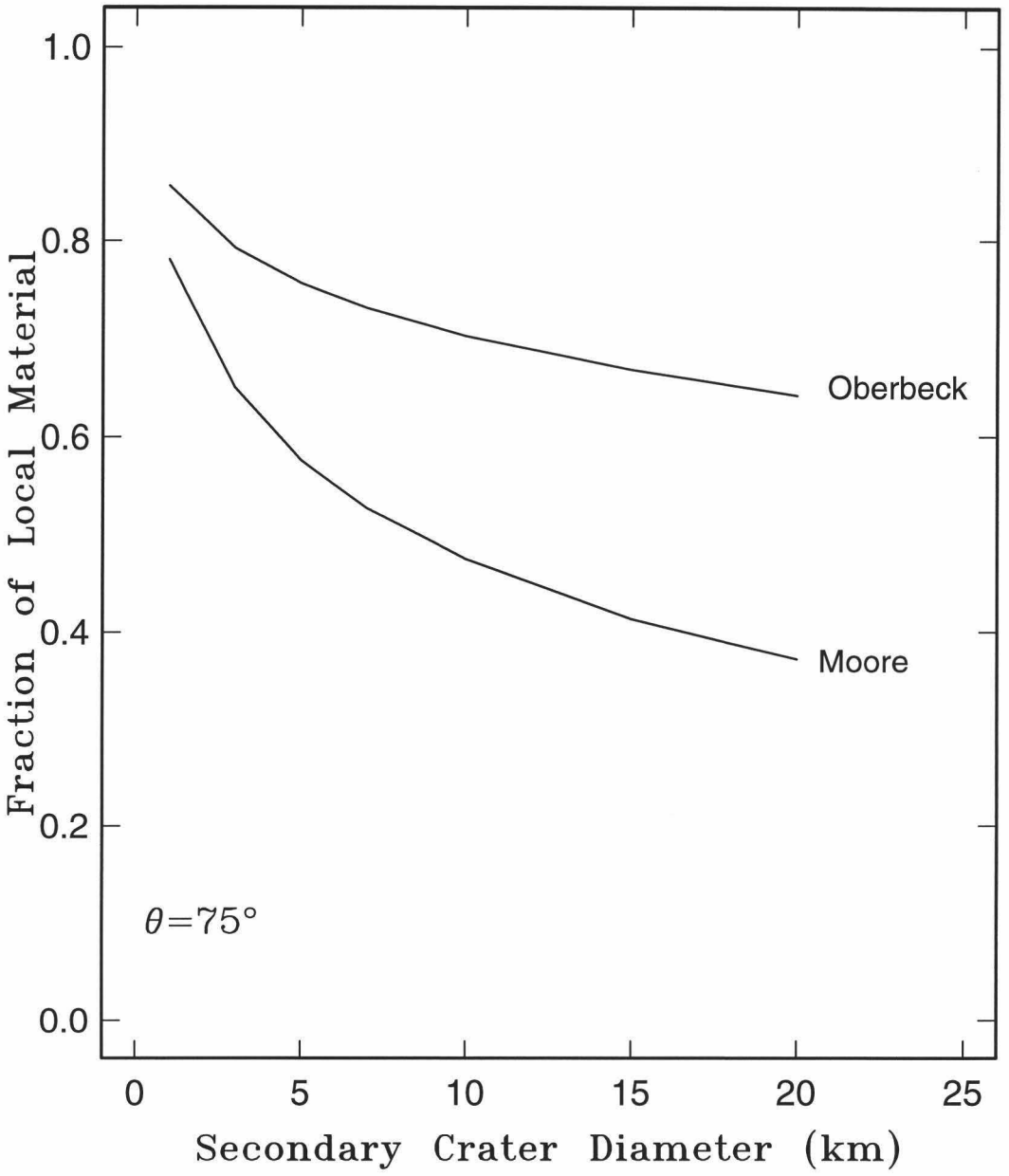

Figure 4.2. Fraction of local material in Orientale-related deposits at the distance of Schickard as a function of secondary-crater diameter, calculated from the relation developed by *Oberbeck et al.* [1975a]. The top curve represents the results from the original Oberbeck equation. The lower curve was computed with the Oberbeck equation modified by a change in the assumed impact scaling law [*Wilhelms*, 1987]. The impact angle in both cases was assumed to be 75° from the vertical.

CHAPTER 5
FINAL REMARKS

5.1 Other Lunar Cryptomaria

The subject of this thesis is the study of cryptomaria and related units in the Schiller-Schickard region. I have also performed studies of other lunar cryptomaria, and will make brief mention of them here.

5.1.1 Northeast Nearside

Occurrences of light plains units are found in the vicinity of Mare Frigoris (e.g., *Lucchitta* [1978]), in the northeastern portion of the Moon's nearside ("NEN" region). Near-IR reflectance spectra were obtained for a number of features in the area. The spectral characteristics of fresh mare material are revealed by spectra for Baily K, a 3 km diameter crater in Mare Frigoris, and for a very small unnamed crater in eastern Frigoris. The Baily K spectrum has a band minimum at 0.95 μm and a depth of 11%, the spectrum of the unnamed crater has a band minimum at 0.98 μm with a depth of 8%. These are typical parameters for fresh mare basalt.

The crater Gärtner D (8 km diam.) is located in the light plains north of Frigoris (unit Ip_2 of *Lucchitta* [1978]), and has a partial dark halo. Two spectra for the interior of this crater were analyzed. The spectral parameters (band minima at 0.97 and 1.00 μm, depths of 8 and 12%) indicate that mare basalt is exposed inside the crater. Therefore, a cryptomare is present. A spectrum for an area of lower-albedo Ip_2 plains east of Frigoris has a band minimum slightly longward of 0.95 μm, and is consistent with the presence of a mare surface contaminated with minor amounts of highlands debris.

The origin of the light plains and cryptomare near Frigoris is not as clear as that of those in the Schiller-Schickard region and requires much more work. The plains

penetrated by Gärtner D are of Imbrian age, and so may be related to the emplacement of ejecta from the Imbrium basin. The plains east of Frigoris may have an origin similar to that of the Schiller-Zucchius plains, namely a mare deposit contaminated by small amounts of highlands material from nearby impacts. The Copernican age craters Thales, Bürg, and Eudoxus as well as other impact structures may have contributed highlands material to the plains east of Frigoris.

Other dark-halo impact craters in the NEN region are found south of Hercules and southeast of Posidonius, in the vicinity of eastern Lacus Somniorum. Spectra of these features demonstrate that mare basalts were exposed by the impacts [*Bell and Hawke*, 1984]. These DHC's are found on the ejecta blankets of larger craters. Therefore the mare basalts were covered by highlands-rich crater ejecta, then re-exposed by later smaller impacts to create the DHC's. A mixing model performed on a set of multispectral images of the Somniorum area confirms that elevated mare abundances are present in surface materials outside of the obvious low-albedo mare deposits.

5.1.2 Crisium Region

The area west and south of the Crisium basin contains several exposures of plains and "smooth terra material" [*Wilhelms,* 1972]. Near-IR reflectance spectra and multispectral images were acquired for a variety of features in the Crisium region, and the results have been discussed by *Blewett et al.* [1994]. Included here is a summary of findings concerning cryptomaria and related units.

Orbital geochemical data, in conjunction with morphological considerations, led to the suggestion that the light plains northeast of Taruntius crater were formed by the extrusion of post-Crisium Basin mare units followed by contamination of these deposits by highlands material [*Hawke and Spudis,* 1980; *Hawke et al.,* 1985]. Spectra for two spots on the plains have band minima longward of 0.95 μm and band depths of 6-7%, clearly indicating a significant mare basalt component. Further evidence for ancient

mare volcanism is provided by the dark-halo impact crater Taruntius C (~12 km diam.) on the northwest rim of Taruntius. A spectrum of this crater has a band minimum of 0.98 μm and a 7% depth, demonstrating that mare basalt was excavated from beneath the deposits of Taruntius.

A triangular patch of plains material is found in the circum-Crisium highlands due north of Taruntius at ~10° N, 46.3° E. A number of factors distinguish this area: it has a low albedo compared to the surrounding highlands and is distinctive in multispectral images (cited by *Wilhelms* [1972]). Additionally, this area possesses a high Mg/Al ratio, similar to that of mare soils, as determined from Apollo orbital geochemical measurements [*Schonfeld,* 1981]. The area corresponds to exposures of Imbrian age (units Ip and Its) on the geological map of the region [*Wilhelms,* 1972]. A reflectance spectrum of the arrowhead plains has a stronger absorption band (~5%) than the nearby highlands massifs, demonstrating a greater abundance of pyroxene in the plains surface. In order to evaluate the possibility of a mare basalt component in the plains, a linear mixing analysis [*Singer and McCord,* 1979] was conducted on the spectrum. The endmembers employed were a mature mare spectrum and a spectrum for a typical mature highlands soil (Apollo 16). The model indicates that a roughly 50-50 mixture of the mare and highlands spectra produce a reasonable fit to the spectrum of the arrowhead plains.

The highlands along the eastern shore of Mare Tranquilitatis contain a distinctive strip of lower albedo material, at ~9.5° N, 43.5° E. This "smooth terra material (Its)" unit has been described as having an uncertain origin, possibly thin mare flows mantling the terra [*Wilhelms,* 1972]. The spectrum obtained for this area has spectral parameters similar to that of the arrowhead plains described above. The relatively strong absorption band indicates a mare basalt component, and a mixing analysis

determined that approximately equal amounts of flux were contributed to this spectrum by mare and highlands spectral types.

5.2 Musings

In the course of this research project I have used several types of data and several analysis techniques to further elucidate the geologic history one of the Moon's most interesting regions. The interpretation of the data has also allowed a greater understanding of one aspect of the most fundamental geologic process altering the surfaces of solid bodies in the Solar System - impact cratering. The results described in this thesis show that the ejecta from basin-size impacts has a profound effect on the pre-existing terrain even at great distances from the impact point. Plains units, widespread across the Moon and once thought to be volcanic in origin, are more likely related to the emplacement of basin ejecta. Mercury also possesses landforms similar to the lunar light plains, and thought has even recently been given to the search for impact deposits on the Earth [*Marshall and Oberbeck,* 1992]. This demonstrates the general importance of understanding the interaction of the ejecta of large impacts with the target substrate.

Although the data used in this thesis was collected before I began study in the Planetary Geosciences Division, I have participated in a number of observing runs at Mauna Kea. Using both the University of Hawaii 88" and 24" telescopes to collect spectral and image data for the Moon, I gained an appreciation for how hard-won any telescopic data is. Unfavorable weather and difficulties with the instrument frequently prevented the observing plan from being carried out.

Telescopic spectra vary widely in quality because of observing conditions (e.g., air mass variations, the shaking of the telescope by wind, atmospheric turbulence or "seeing", variable cloud and atmospheric water vapor conditions), instrument performance, and the nature of the target. However, in performing the many band analyses described in this work, I discovered that the analysis technique is quite robust.

In the trial and error process of fitting the "1 μm" absorption band, several attempts are made to fit a cubic polynomial to slightly different portions of the band. I found that the band parameters (in particular and most importantly the location of the band minimum) are not strongly sensitive to the particular number of points (channels) used in the fit. The presence of more noise in some spectral data should not greatly affect the usefulness of that data.

The experience I have gained while working on the Schiller-Schickard project has been excellent preparation for my upcoming Ph.D. research. The recent completion of the *Clementine 1* mission has provided a global image data set in 5 colors in the UV/visible and 6 in the near IR, and a near-global set of laser altimetric measurements. Image processing skills developed while analyzing the Earth-based telescopic CCD images will serve me well in the utilization of *Clementine* data. The spacecraft returned on the order of 1.5 million images, so producing images cubes by registering mosaics of images taken through different filters will be a major task. Images recorded by the *Galileo* spacecraft's imaging systems during the 1990 and 1992 lunar flybys, and rehabilitated *Mariner 10* [*Robinson et al.*, 1992] images will serve as supplements to the superb *Clementine* data set. The *Clementine* data will no doubt revolutionize our knowledge of the Moon's composition and history.

Clementine has opened the farside to the compositional studies possible with multispectral imaging. The nearside was also completely covered by the spacecraft's cameras. However, there is still an important role for Earth-based spectral observation of the Moon. It is likely that interesting areas will be identified in *Clementine* data, but that the spectral resolution will be too low to completely characterize the mineralogy of the surface. By performing high spectral resolution observations of the key areas, detailed mineralogical information can be obtained and tied in to the image data.

Alternately, a global high spatial resolution imaging spectrometer data set could provide the high spectral resolution information needed for mineralogical mapping. However, the availability of quality *Clementine* multispectral images has probably weakened the justification for including an imaging spectrometer on missions in the foreseeable future.

The other key type of remote sensing observation needed to complement the spectral data is the chemical information provided by X-ray and γ-ray spectrometers in polar orbit about the Moon. Hopefully instruments of this type will be flown in either a NASA *Discovery*-type mission, or by a military-NASA joint venture such as *Clementine*. The availability of data of this type should permit great strides in the knowledge of the origin and geologic history of this important endmember terrestrial planet.

APPENDIX A

DATES AND ORIGINAL NAMES OF NEAR-IR SPECTRA

Table A.1. Spectral parameters and original names of spectra.

Spectrum ID no.	SPOT	Original Name of Spectrum, Date Collected	Band min.	Contin. slope	Band depth	FWHM*	Asymm.
4	Schiller-Zuc Plains S	Schill LP S 23jan81	0.959	0.627	0.060	0.352	0.651
5	Schiller-Zuc Plains N	Schill LP N 23jan81	0.980	0.625	0.060	0.280	0.894
6	Schiller-Zuc Plains #3	False LP 17aug81	0.950	0.676	0.066	0.261	0.631
7	Schiller floor	Schill floor 17aug81	0.929	0.604	0.061	0.248	0.610
8	Noggerath F bowl #1	Nogg F bowl 14sept81	0.975	0.529	0.217	0.280	0.786
9	Noggerath F bowl #2	Nogg F bowl 15aug81	0.969	0.496	0.205	0.276	0.827
10	Noggerath F bowl #3	Nogg F bowl 16aug81	0.976	0.551	0.189	0.281	0.871
12	Nogg F ejecta #1	Nogg F ejecta 15aug81	0.978	0.662	0.112	0.253	0.932
13	Nogg F ejecta #2	Nogg F ejecta 16aug81	0.969	0.666	0.120	0.248	0.750
14	Nogg F ejecta #3	Nogg F ejecta 14sept81	0.991	0.650	0.084	0.223	1.159
15	Drebbel F ejecta #1	Drebbel F ejecta 23jan81	0.948	0.644	0.061	0.260	0.667
16	Drebbel F ejecta #2	Drebbel F ejecta 17aug81	0.976	0.664	0.068	0.264	0.926
17	Drebbel F ejecta #3	Drebbel F ejecta 14sept81	0.954	0.667	0.050	0.213	0.947
18	Inghirami W	Inghirami W 30jun80	0.976	0.661	0.071	0.277	0.854
19	Inghirami W bowl #1	Inghirami W bowl 17aug81	0.985	0.602	0.106	0.264	1.140
20	Inghirami W bowl #2	Inghirami W bowl 14sept81	0.946	0.590	0.141	0.291	0.719
21	Wargentin DHC	Wargentin DHC 17aug81	0.994	0.646	0.052	0.282	1.529
22	Lacus Excellentiae	Puddle 1 23jan81	0.973	0.640	0.076	0.287	0.777
23	Schickard mare N #1	Schickard mare N 23jan81	0.970	0.691	0.086	0.288	0.721
24	Schickard mare N #2	Schickard mare N 16aug81	0.962	0.702	0.083	0.229	0.759
25	Schickard mare N #3	Schickard mare N 14sept81	0.978	0.695	0.082	0.251	1.038
26	Schickard mare crater #1	Schick mare crater 17aug81	0.961	0.641	0.148	0.269	0.831
27	Schickard mare crater #2	Schick mare crater 14sept81	0.989	0.611	0.133	0.292	1.338
28	Schickard mare S	Schick mare S 23jan81	0.996	0.690	0.088	0.292	0.773
30	Schickard X #1	Schick X 23jan81	0.958	0.526	0.062	0.326	0.802
31	Schickard X #2	Schick X 16aug81	0.920	0.486	0.053	0.189	0.871
33	Schickard R	Schick R 30jun80	0.976	0.672	0.095	0.276	0.842
34	Schickard center	Schick center 23jan81	0.944	0.630	0.048	0.298	0.774
35	Schickard LP #1	Schick LP 16aug81	0.935	0.605	0.051	0.222	0.657
36	Schickard LP #2	Schick LP 14sept81	0.956	0.598	0.048	0.228	0.900
37	Schickard LP crater #1	Schick LP crater 17aug81	0.959	0.436	0.201	0.270	0.862
38	Schickard LP crater #2	Schick br crater 23jan81	0.962	0.618	0.120	0.327	0.807
40	Schiller-Zuc Plains #4	LP N of Zucchius 19aug89	0.955	0.595	0.081	0.287	0.789
41	Schiller-Zuc Plains #5	LP N Zucchius #2 20aug89	0.952	0.654	0.073	0.266	0.482

*Band full width at half-maximum

APPENDIX B

COMPUTER PROGRAM TO PERFORM PRINCIPAL COMPONENTS ANALYSIS

```
PRO prcomp
;
;  IDL code to perform principal components analysis on a group of spectra. ;
;        The procedure first calculates the variance-covariance matrix
;             for the group of spectra, then extracts eigenvalues and
;             eigenvectors, and calculates the pc scores of the
;             original data.
;
;             The spectra read in by this program must be in a file
;             arranged so that each spectrum is a line (row), with the
;             reflectances at each wavelength as the samples (columns).
;             Reference: Eqn. 2.22 of Davis(1986) Stat. & Data
;             Analy. in Geology.
;
;             DTB Nov 1992
;
;23456789
        dfil=''
        outp=''
        eval=''
        evec=''
        scnam=''
        print,''
        print,'IDL procedure PRCOMP'
        print,''
        read,'Give the name of the file containing the spectra: ',dfil
        read,'How many spectra? ',ns
        read,'How many channels in the spectra? ',nch
        read,'Give a name for the output var-covar matrix file: ',outp
        print,''
        read,'Give a name for the eigenvalue file: ',eval
        read,'Give a name for the eigenvector file: ',evec
        read,'Give a name for the pc scores file: ',scnam
        print,''
;        nch=8
;        ns=5
; read in the data file
        dat1=fltarr(nch,ns)
        openr,21,dfil
           readu,21,dat1              ;readu for reading binary raster
        close,21
;
; calculate the var-covar matrix
        print,'Calculating variance-covariance matrix...'
        print,''
        cov=fltarr(nch,nch)
        nc=nch-1
```

```
        nsp=ns-1
        for in1=0, nc do begin
              for in2=0, nc do begin
                    sum1=0.0
                    sum2=0.0
                    sumcp=0.0
                    for is=0, nsp do begin
                  sum1=sum1+dat1(in1,is)
                  sum2=sum2+dat1(in2,is)
                          sumcp=sumcp+(dat1(in1,is)*dat
                  1(in2,is))  endfor
                  p1=ns*sumcp
                  d1=p1-(sum1*sum2)
                  covar=d1/(ns*(ns-1))
                  cov(in2,in1)=covar
              endfor
        endfor
; calculate mean for each band
;         mean=fltarr(nch)
;        for iband=0,nch-1 do begin
;           mean(iband) = total(dat1(*,iband))/ns
;           print,'band ',iband+1,' mean ',mean(iband)
;        endfor
;
;
; calculate the covariance matrix
;         temp=fltarr(ns,nch)
;        for i=0, nch-1 do begin
;           for j=0, nch-1 do begin
;                    sum=0.0
;                    for isamps=0, ns-1 do begin
;                                sum=(dat1(isamps,i)-mean(i))*(dat1(isamps,j)-mean(j))+sum
;                   endfor
;                       cov(j,i)=(sum*1.)/(ns-1.0)
;           endfor
;        endfor
;
        openw,22,outp
           printf,22,cov(*,*)
        close,22
;
; extract eigenvalues and eigenvectors
; TRED2 is a procedure to reduce a symmetric matrix to tridiagonal form,
;    based on a routine of the same name in Numerical Recipes in C.
;    TQLI is a procedure to determine the eigenvals and eigenvects of a
;    symmetric triadiagonal matrix, based on a routine of the same name in
;    Numerical Recipes in C. See the IDL User's Guide.
;
        covm=fltarr(nch,nch)
        d1=fltarr(nch)
        e1=fltarr(nch)
        covm=cov
```

```
        tred2,covm,d1,e1
        tqli,d1,e1,covm
;
; d1 contains the eigenvalues, covm now contains the eigenvectors, however,
;    they are in the 'wrong' order, so reverse them
;
        k=(nch-1)
        d2=fltarr(nch)
        ev=fltarr(nch,nch)
        for ia=0,k do begin
              for ib=0,k do begin
                   k1=k-ib
                   d2(ib)=d1(k1)
                   ev(ia,ib)=covm(ia,k1)
              endfor
        endfor
        evb=fltarr(nch,nch)
        evb=transpose(ev)
;
; I tested this program using data from Davis tables 6.18 and 6.21
;    The eigenvectors as calculated have the opposite sign of the evects
;    in the Davis example, so to stay consistent with Davis, change the
;    sign of the eigenvectors.
;
        evc=-evb
;
        print,''
;    write the eigenvalues and eigenvectors to files
        openw,51,eval
           printf,51,d2
        close,51
        openw,52,evec
           printf,52,evc
        close,52
;
;       sum the eigenvalues and calculate % of var. for 1st 4 PC's
;
        sumval=total(d2)  ; total sums all elements of the array
        v=fltarr(4)  ; change this later to 4
        for i1=0,3 do begin   ; change this to 0,3 also
             v(i1)=100.0*d2(i1)/sumval
             print,'Eigenvalue',i1+1,' =',d2(i1),' ->  PC',i1+1,$
             ' contains',v(i1),'% of variance'
        endfor
;
;23456789
;       compute the 1st 3 PC scores of each spectrum,
;         see Davis, p. 531.  Orig. data must be arranged so that
;         each spectrum is a row, with the channels as the columns
;
         sc=fltarr(3,ns)    ;change to 3
        sc(*,*)=0
```

```
k2=(ns-1)
for i2=0,k2 do begin
    for i3=0,k do begin
        sc(0,i2)=sc(0,i2)+evc(0,i3)*da
        t1(i3,i2)
        sc(1,i2)=sc(1,i2)+evc(1,i3)*da
        t1(i3,i2)
        sc(2,i2)=sc(2,i2)+evc(2,i3)*da
        t1(i3,i2)

                              endfor
        endfor
    ;
    ;
    ;   write PC scores to a file
    ;
        openw,23,scnam
              printf,23,sc(*,*)
        close,23
    ;
    ;
        print,''
    ;
        stop
        end
    ;
```

REFERENCES

Adams, J. B., Visible and near-infrared diffuse reflectance spectra of pyroxenes as applied to remote sensing of solid objects in the solar system, *J. Geophys. Res.* **79**, no. 32, 4829-4836, 1974.

Adams, J. B., M. O. Smith and P. E. Johnson, Spectral mixture modeling: A new analysis of rock and soil types at the Viking Lander 1 site, *J. Geophys. Res.* **91**, no. B8, 8098-8112, 1986.

Antonenko, I. and J. W. Head, Cryptomaria in the Schiller-Schickard, Mare Humorum, and western Oceanus Procellarum area: Studies using dark-halo craters, *Lunar Planet. Sci. XXV*, 35-36, 1994.

Bastin, J. A., A new theory for the formation of the maria and Cayley type lunar regions, *Moon* **10**, 143-162, 1974.

Bell, J. F. and B. R. Hawke, Lunar dark-haloed impact craters: Origin and implications for early mare volcanism, *J. Geophys. Res.* **89**, 6899-6910, 1984.

Belton, M. J. S. and the Galileo SSI team, Lunar impact basins and crustal heterogeneity: New western limb and farside data from Galileo, *Science* **255**, 570-576, 1992.

Blewett, D. T., B. R. Hawke, P. G. Lucey, and P. D. Spudis, A spectral survey of the Crisium region of the Moon, *Lunar Planet. Sci. XXV*, 127-128, 1994.

Blewett, D. T., B. R. Hawke, P. G. Lucey, J. F. Bell, G. J. Taylor, C. A. Peterson and P. D. Spudis, A detailed spectral study of the Schiller-Schickard region of the Moon, *Bull. Am. Astron. Soc.* **23**, no. 3, 1200, 1991.

Blewett, D. T., B. R. Hawke, P. G. Lucey, J. F. Bell III, R. Jaumann, H. Hiesinger, G. Neukum and P. D. Spudis, Spectral and multispectral imaging studies of lunar mantled mare deposits, *Lunar Planet Sci. XXIV*, 133-134, 1993.

Blewett, D. T., B. R. Hawke, P. G. Lucey, J. F. Bell III, J. F. Bell, G. J. Taylor, C. A. Peterson and P. D. Spudis, A near-IR spectral investigation of the Schiller-Schickard region of the Moon, *Lunar Planet. Sci. XXIII*, 123-124, 1992.

Chao, E. C. T., Impact cratering models and their application to lunar studies - a geologist's view, *Proc. Lunar Planet. Sci. Conf. 5th* , 35-52, 1974.

Clark, R. N., A large scale interactive one-dimensional array processing system, *Publ. Astron. Soc. Pac.* **92**, 221-224, 1980.

Davis, J. C., *Statistics and Data Analysis in Geology,* John Wiley & Sons, New York, 1986.

Deutsch, A. and D. Stöffler, Rb-Sr analyses of Apollo 16 melt rocks and a new age estimate for the Imbrium basin: Lunar basin chronology and the early heavy bombardment of the Moon, *Geochim. Cosmochim. Acta* **51**, 1951-1964, 1987.

Echo & the Bunnymen, "The Killing Moon", *Ocean Rain*, Sire Records, 1984.

Eggleton, R. E. and G. G. Schaber, "Cayley formation interpreted as basin ejecta," in *Apollo 16 Preliminary Science Report,* NASA SP-315, pp. 29-7 - 29-16, 1972.

Greeley, R. et al., Galileo imaging observations of lunar maria and related deposits, *J. Geophys. Res.* **98**, no. E9, 17183-17205, 1993.

Hackman, R. J., Geologic map of the Montes Apenninus Region, U. S. Geol. Survey Map I-463, 1966.

Hartmann, W. K. and G. P. Kuiper, Concentric structures around lunar basins, *Comm. Lunar Planet. Lab.* **1**, no. 12, 51-66, 1962.

Hartmann, W. K. and C. A. Wood, Moon: origin and evolution of multi-ring basins, *Moon* **3**, no. 1, 3-78, 1971.

Hawke, B. R., P. D. Spudis, and P. E. Clark, The origin of selected lunar geochemical anomalies: Implications for early volcanism and the formation of light plains, *Earth, Moon, Planets* **32**, 257-273, 1985.

Hawke, B. R. and J. F. Bell, Remote sensing studies of lunar dark-halo impact craters: Preliminary results and implications for early volcanism, *Proc. Lunar Planet. Sci. Conf. 12th*, 665-678, 1981.

Hawke, B. R. and J. W. Head, Lunar KREEP volcanism: Geologic evidence for history and mode of emplacement, *Proc. Lunar Planet. Sci. Conf. 9th*, 3285-3309, 1978.

Hawke, B. R., P. G. Lucey, G. J. Taylor, P. D. Spudis, J. F. Bell, C. A. Peterson, D. Blewett and K. Horton, Remote sensing studies of the Orientale region of the Moon: A pre-Galileo view, *Geophys. Res. Lett.* **18**, no. 11, 2141-2144, 1991.

Hawke, B. R. and P. D. Spudis, Geochemical anomalies on the eastern limb and farside of the Moon, *Proc. Conf. Lunar Highlands Crust*, 467-481, 1980.

Head, J. W., Orientale multi-ringed basin interior and implications for the petrogenesis of lunar highland samples, *Moon* **11**, 327-356, 1974.

Head, J. W. and B. R. Hawke, Geology of the Apollo 14 region (Fra Mauro): Stratigraphic history and sample provenance, *Proc. Lunar Sci. Conf. 6th*, 2483-2501, 1975.

Head, J. W., S. Murchie, J. F. Mustard, C. M. Pieters, G. Neukum, A. McEwen, R. Greeley, E. Nagel and M. J. S. Belton, Lunar impact basins: New data for the western limb and far side (Orientale and South Pole-Aitken Basins) from the first Galileo flyby, *J. Geophys. Res.* **98**, no. E9, 17149-17181, 1993a.

Head, J. W., J. Mustard, I. Antonenko and B. R. Hawke, Modes of formation of lunar light plains and the detection of cryptomaria deposits, *Lunar Planet. Sci. XXIV*, 629-630, 1993b.

Head, J. W. and L. Wilson, Lunar mare volcanism: Stratigraphy, eruption conditions, and the evolution of secondary crusts, *Geochim. Cosmochim. Acta* **56**, 2155-2175, 1992.

Jaumann, R., Spectral-chemical analysis of lunar surface materials, *J. Geophys. Res.* **96**, no. E5, 22793-22807, 1991.

Johnson, P. E., M. O. Smith and J. B. Adams, Quantitative analysis of planetary reflectance spectra with principal components analysis, *Proc. Lunar Planet. Sci. Conf. 15th, J. Geophys. Res.* **90**, supplement, C805-C810, 1985.

Karlstrom, T. N. V., Geologic map of the Schickard quadrangle of the Moon, U. S. Geol. Survey Map I-823, 1974.

Kruse, F. A., A. B. Lefkoff, J. W. Boardman, K. B. Heidebrecht, A. T. Shapiro, P. J. Barloon and A. F. H. Goetz, The Spectral Image Processing System (SIPS) - Interactive visualization and analysis of imaging spectrometer data, *Remote Sens. Environ.* **44**, 145-163, 1993.

Lucchitta, B. K., Geologic map of the north side of the Moon, U. S. Geol. Survey Map I-1062, 1978.

Lucey, P. G., B. R. Hawke, C. M. Pieters, J. W. Head and T. B. McCord, A compositional study of the Aristarchus region of the Moon using near-infrared reflectance spectroscopy, *Proc. Lunar Planet. Sci. Conf. 16th, J. Geophys. Res.* **91**, no. B4, D344-D354, 1986.

Marshall, J. R. and V. R. Oberbeck, Textures of impact deposits and the origin of tillites, *Eos* **73**, no. 43 (suppl.), 324, 1992.

McCord, T. B., R. N. Clark, B. R. Hawke, L. A. McFadden, P. D. Owensby, C. M. Pieters and J. B. Adams, Moon: Near-infrared spectral reflectance, a first good look, *J. Geophys. Res.* **86**, no. B11, 10883-10892, 1981.

McEwen, A. S., L. R. Gaddis, G. Neukum, H. Hoffman, C. M. Pieters and J. W. Head, Galileo observations of post-Imbrium craters during the first Earth-Moon flyby, *J. Geophys. Res.* **98**, no. E9, 17207-17231, 1993.

Milton, D. J. and C. A. Hodges, Geologic maps of the Descartes region of the Moon, U. S. Geol. Survey Map I-748, 1972.

Moore, H. J., C. A. Hodges and D. H. Scott, Multiringed basins - illustrated by Orientale and associated features, *Proc. Lunar Sci. Conf. 5th*, 71-100, 1974.

Morrison, R. H. and V. R. Oberbeck, Geomorphology of crater and basin deposits: Emplacement of the Fra Mauro formation, *Proc. Lunar Sci. Conf. 6th*, 2503-2530, 1975.

Mustard, J. F., J. W. Head, S. M. Murchie, C. M. Pieters, M. S. Belton and A. S. McEwen, Schickard cryptomare: Interaction between Orientale ejecta and pre-basin mare from spectral mixture analysis of Galileo SSI data, *Lunar Planet. Sci. XXIII*, 957-958, 1992.

Neukum, G., R. Jaumann, H. Hoffman, J. Oberst, R. Wagner, P. Regner, H. Rebhan, H. Hiesinger and A. Dummel, Earth-based multispectral observations of the Moon, *Lunar Planet. Sci. XXII*, 971-972, 1991.

Oberbeck, V. R., The role of ballistic erosion and sedimentation in lunar stratigraphy, *Rev. Geophys. Space Phys.* **13**, no. 2, 337-362, 1975.

Oberbeck, V. R., F. Hörz, R. H. Morrison, W. L. Quaide and D. E. Gault, On the origin of the lunar smooth-plains, *Moon* **12**, 19-54, 1975a.

Oberbeck, V. R., R. H. Morrison and F. Hörz, Transport and emplacement of crater and basin deposits, *Moon* **13**, 9-26, 1975b.

Oberbeck, V. R., R. H. Morrison, F. Hörz, W. L. Quaide and D. E. Gault, Smooth plains and continuous deposits of craters and basins, *Proc. Lunar Sci. Conf. 5th, Geochim. Cosmochim. Acta*, supplement 5, 111-136, 1974.

Offield, T. W., Geologic map of the Schiller quadrangle of the Moon, U. S. Geol. Survey. Map I-691, 1971.

Pieters, C. M., J. B. Adams, P. J. Mouginis-Mark, S. H. Zisk, M. O. Smith, J. W. Head and T. B. McCord, The nature of crater rays: The Copernicus example, *J. Geophys. Res.* **90**, no. B14, 12393-12413, 1985.

Pieters, C. M. et al., Crustal diversity of the Moon: Compositional analyses of Galileo solid state imaging data, *J. Geophys. Res.* **98**, no. E9, 17127-17148, 1993.

Pike, R. J., Depth/diameter relations of fresh lunar craters: Revision from spacecraft data, *Geophys. Res. Lett.* **1**, no. 7, 291-294, 1974.

Pohn, H. A. and R. L. Wildey, A photoelectric-photographic study of the normal albedo of the Moon, U. S. Geol. Survey Prof. Paper 599-E, 1970.

Robinson, M. S., B. R. Hawke, P. G. Lucey and G. A. Smith, Mariner 10 multispectral images of the eastern limb and farside of the Moon, *J. Geophys. Res.* **97**, no. E11, 18265-18274, 1992.

Schonfeld, E., High spatial resolution Mg/Al maps of the western Crisium and Sulpicius Gallus regions, *Proc. Lunar. Planet. Sci. Conf. 12th*, 809-816, 1981.

Schultz, P. H. and D. E. Gault, Seismic effects from major basin formations on the Moon and Mercury, *Moon* **12**, 159-177, 1975.

Schultz, P. H. and D. E. Gault, Clustered impacts: Experiments and interpretations, *J. Geophys. Res.* **90**, no. B5, 3701-3732, 1985.

Schultz, P. H. and P. D. Spudis, Evidence for ancient mare volcanism, *Proc. Lunar Planet. Sci. Conf. 10th*, 2899-2918, 1979.

Schultz, P. H. and P. D. Spudis, Beginning and end of lunar mare volcanism, *Nature* **302**, 233-236, 1983.

Singer, R. B. and T. B. McCord, Mars: Large scale mixing of bright and dark surface materials and implications for analysis of spectral reflectance, *Proc. Lunar Planet. Sci. Conf. 10th*, 1835-1848, 1979.

Smith, M. O., P. E. Johnson and J. B. Adams, Quantitative determination of mineral types and abundances from reflectance spectra using principal components analysis, *Proc. Lunar Planet. Sci. Conf. 15th, J. Geophys. Res.* **90**, supplement, C797-C804, 1985.

Solomon, S. C., Mare volcanism and lunar crustal structure, *Proc. Lunar Sci. Conf. 6th*, 1021-1042, 1975.

Spudis, P. D., Composition and origin of the Apennine Bench Formation, *Proc. Lunar Planet. Sci. Conf. 9th*, 3379-3394, 1978.

Spudis, P. D., B. R. Hawke and P. G. Lucey, Geology and deposits of the Imbrium basin, *Proc. Lunar Planet. Sci. Conf. 18th*, 155-168, 1988.

Stöffler, D., D. E. Gault, J. Wedekind and G. Polkowski, Experimental hypervelocity impact into quartz sand: Distribution and shock metamorphism of ejecta, *J. Geophys. Res.* **80**, 4062-4077, 1975.

Taylor, S. R., Growth of planetary crusts, *Tectonophysics* **161**, 147-156, 1989.

Vega, S., "Small Blue Thing", *Suzanne Vega*, A&M Records, 1985.

Whitaker, E. A., G. P. Kuiper, W. K. Hartmann and L. H. Spradley, *Rectified Lunar Atlas,* Aeronautical Chart and Information Center, St. Louis, 1963.

Wildey, R. L., A digital file of the lunar normal albedo, *Moon* **16**, 231-277, 1977.

Wilhelms, D., The Geologic History of the Moon, 1987.

Wilhelms, D. E., Geologic map of the Taruntius quadrangle of the Moon, U. S. Geol. Survey. Map I-722, 1972.

Wilhelms, D. E., Mercurian volcanism questioned, *Icarus* **28**, 551-558, 1976.

Wilhelms, D. E. and J. F. McCauley, Geologic map of the nearside of the Moon, U. S. Geol. Survey Map I-703, 1971.